Monthly Notices of the ROYAL ASTRONOMICAL SOCIETY

MNRAS **516,** 1193–1218 (2022) https://doi.org/10.1093/mnras/stac2218
Advance Access publication 2022 August 6

The Zwicky Transient Facility phase I sample of hydrogen-rich superluminous supernovae without strong narrow emission lines

T. Kangas [1]★ Lin Yan,[2] S. Schulze [3] C. Fransson,[4] J. Sollerman,[4] R. Lunnan,[4] C. M. B. Omand,[4] I. Andreoni,[5,6,7] R. Burruss,[8] T.-W. Chen,[4] A. J. Drake,[9] C. Fremling,[9] A. Gal-Yam,[10] M. J. Graham [9] S. L. Groom,[11] J. Lezmy,[12] A. A. Mahabal [9,13] F. J. Masci,[11] D. Perley [14] R. Riddle [2] L. Tartaglia[4,15] and Y. Yao[16]

[1]*Department of Physics, KTH Royal Institute of Technology, The Oskar Klein Centre, AlbaNova, SE-106 91 Stockholm, Sweden*
[2]*The Caltech Optical Observatories, California Institute of Technology, Pasadena, CA 91125, USA*
[3]*Department of Physics, The Oskar Klein Centre, Stockholm University, AlbaNova, SE-106 91 Stockholm, Sweden*
[4]*Department of Astronomy, The Oskar Klein Centre, Stockholm University, AlbaNova, SE-106 91 Stockholm, Sweden*
[5]*Joint Space-Science Institute, University of Maryland, College Park, MD 20742, USA*
[6]*Department of Astronomy, University of Maryland, College Park, MD 20742, USA*
[7]*Astrophysics Science Division, NASA Goddard Space Flight Center, Mail Code 661, Greenbelt, MD 20771, USA*
[8]*Caltech Optical Observatories, California Institute of Technology, 35899 Canfield Road Palomar Mountain, CA 92060-0200, USA*
[9]*Division of Physics, Mathematics, and Astronomy, California Institute of Technology, Pasadena, CA 91125, USA*
[10]*Department of Particle Physics and Astrophysics, Weizmann Institute of Science, 76100 Rehovot, Israel*
[11]*IPAC, California Institute of Technology, 1200 E. California Blvd, Pasadena, CA 91225, USA*
[12]*Université de Lyon, Université Claude Bernard Lyon 1, CNRS/IN2P3, IP2I Lyon, F-69622 Villeurbanne, France*
[13]*Center for Data Driven Discovery, California Institute of Technology, Pasadena, CA 91125, USA*
[14]*Astrophysics Research Institute, Liverpool John Moores University, 146 Brownlow Hill, Liverpool L3 5RF, UK*
[15]*INAF - Osservatorio Astronomico di Padova, Vicolo dell'Osservatorio 5, I-35122 Padova, Italy*
[16]*Cahill Center for Astronomy and Astrophysics, California Institute of Technology, Pasadena, CA 91125, USA*

Accepted 2022 August 2. Received 2022 July 22; in original form 2022 April 11

ABSTRACT

We present a sample of 14 hydrogen-rich superluminous supernovae (SLSNe II) from the Zwicky Transient Facility (ZTF) between 2018 and 2020. We include all classified SLSNe with peaks $M_g < -20$ mag with observed *broad* but not narrow Balmer emission, corresponding to roughly 20 per cent of all hydrogen-rich SLSNe in ZTF phase I. We examine the light curves and spectra of SLSNe II and attempt to constrain their power source using light-curve models. The brightest events are photometrically and spectroscopically similar to the prototypical SN 2008es, while others are found spectroscopically more reminiscent of non-superluminous SNe II, especially SNe II-L. ^{56}Ni decay as the primary power source is ruled out. Light-curve models generally cannot distinguish between circumstellar interaction (CSI) and a magnetar central engine, but an excess of ultraviolet (UV) emission signifying CSI is seen in most of the SNe with UV data, at a wide range of photometric properties. Simultaneously, the broad Hα profiles of the brightest SLSNe II can be explained through electron scattering in a symmetric circumstellar medium (CSM). In other SLSNe II without narrow lines, the CSM may be confined and wholly overrun by the ejecta. CSI, possibly involving mass lost in recent eruptions, is implied to be the dominant power source in most SLSNe II, and the diversity in properties is likely the result of different mass loss histories. Based on their radiated energy, an additional power source may be required for the brightest SLSNe II, however – possibly a central engine combined with CSI.

Key words: transients: supernovae – stars: magnetars – stars: mass-loss – galaxies: statistics.

1 INTRODUCTION

Massive stars ($\gtrsim$8 M$_\odot$) end their lives in supernova (SN) explosions. In addition to ordinary core-collapse SNe (CCSNe), wide-field, untargeted transient searches have also uncovered classes of superluminous SNe (SLSNe; for reviews see Gal-Yam 2012, 2019); these are analogous to hydrogen-poor (i.e. Type I) and hydrogen-rich (Type II) CCSNe, but reach peak absolute magnitudes $\lesssim -20$ mag (e.g. Quimby et al. 2011; De Cia et al. 2018; Chen et al. 2022a), even possibly ~ -23 mag (Dong et al. 2016; Li et al. 2020) – but see also Leloudas et al. (2016). The source of this unusual luminosity is as yet debated. Mechanisms commonly considered for SLSNe include the decay of ^{56}Ni synthesized in the SN explosion, requiring amounts of ^{56}Ni unattainable except in pair-instability SNe (PISNe) of extremely massive stars (Barkat, Rakavy & Sack 1967; Heger & Woosley 2002); interaction with the circumstellar medium (CSM) efficiently converting the kinetic energy of the ejecta into radiation

★ E-mail: tjakangas@gmail.com

(e.g. Chevalier & Fransson 1994; Ofek et al. 2007; Sorokina et al. 2016); and a central engine such as a strongly magnetized, fast-spinning neutron star born in the collapse – a millisecond magnetar – that provides additional energy to the ejecta (Kasen & Bildsten 2010; Woosley 2010). Another possible central engine is fallback accretion on to a nascent black hole (Dexter & Kasen 2013). Depending on the mechanism, SLSNe are generally thought to require very massive progenitors (whether single or binary), initially on the order of $\gtrsim$30 $M_\odot$ or even $\gtrsim$100 $M_\odot$ (e.g. Jerkstrand et al. 2017; Lunnan et al. 2018; Stevance & Eldridge 2021).

Type I SLSNe have been studied more extensively in the literature than Type II, owing to more abundant observational data (see e.g. Moriya, Sorokina & Chevalier 2018; Quimby et al. 2018; Chen et al. 2022a). A magnetar central engine is commonly invoked as the power source (e.g. Nicholl et al. 2013, 2015; Inserra et al. 2013b), although circumstellar interaction (CSI) is a better match to some SLSNe I (Lunnan et al. 2018; Chen et al. 2022b). Undulations in SLSN light curves (Chen et al. 2017; Inserra et al. 2017) are often best explained by CSI (see e.g. West et al. 2022) despite the lack of strong narrow emission lines, but variations in the central engine remain a plausible mechanism for some objects as well (e.g. Chugai & Utrobin 2022; Moriya et al. 2022; Chen et al. 2022b)

Type II SLSNe, the prototype of which is SN 2006gy (Ofek et al. 2007; Smith et al. 2007), mostly exhibit classic Type IIn spectra, and can be considered simply the bright end of the Type IIn luminosity function (e.g. Perley et al. 2016). These 'SLSNe IIn' are most likely powered by CSI. There are, however, SLSNe II without strong narrow lines as well. The prototype of this hitherto small group of events is SN 2008es (Gezari et al. 2009; Miller et al. 2009), which bore a strong similarity to linearly declining SNe II, historically called SNe II-L (Barbon, Ciatti & Rosino 1979). Typical SNe II-L have recently been considered analogous to the fainter, slower SNe II-P (Valenti et al. 2015), but with more massive progenitors (possibly 15–20 $M_\odot$; van Dyk et al. 1999; Faran et al. 2014; Kangas et al. 2017), higher mass-loss rates, less hydrogen in the ejecta and therefore a short or non-existent plateau phase (Anderson et al. 2014; Bose et al. 2018; Reynolds et al. 2020).

A subset of SNe II-L, such as SN 1979C and SN 2013fc, are unusually luminous, reaching peak absolute magnitudes of ~-20 mag (Panagia et al. 1980; de Vaucouleurs et al. 1981; Kangas et al. 2016). SN 1998S (e.g. Leonard et al. 2000; Fassia et al. 2001) and a few other SNe IIn are similar to these and could be considered SNe II-L with early or weak narrow lines (Inserra et al. 2013a; Taddia et al. 2013; Tartaglia et al. 2021). While the light curves of most SNe II seem to require some early CSI (Morozova, Piro & Valenti 2018), the properties of the luminous SNe II-L suggest that stronger CSI is responsible for boosting their luminosity above that of normal SNe II (e.g. Kangas et al. 2016). CSI has also been suggested to power the prototypical broad-lined SLSN II, SN 2008es, which resembles a SN II-L, but with a 15–20 d delay in its spectroscopic evolution, somewhat weaker absorption lines and a broader light curve (Gezari et al. 2009; Miller et al. 2009).

Inserra et al. (2018) studied SN 2008es and two other SLSNe II that lacked strong narrow emission lines. Until now, these three SNe and CSS121015 (Benetti et al. 2014) have been the only such SNe known in the literature. Following Inserra et al. (2018) and Gal-Yam (2019), for the purposes of this paper, we will use the term 'SLSNe II' to refer to only such SNe. SLSNe with strong narrow Balmer lines will be called SLSNe IIn. A magnetar central engine, analogous to those possibly powering SLSNe I, was found compatible with SLSN II light curves and temperatures by Inserra et al. (2018). On the other hand, CSI can produce a variety of emission-line profiles, not necessarily narrow (e.g. Moriya & Tominaga 2012; McDowell, Duffell & Kasen 2018; Taddia et al. 2020). Late-time observations of SN 2008es favoured the CSI scenario, but a magnetar central engine has not been excluded as the *dominant* power source of SLSNe II (Bhirombhakdi et al. 2019). The host galaxies of the known members of this subclass are similar to those of SLSNe I (Inserra et al. 2018), i.e. blue, faint and metal-poor (while SLSNe IIn show a wider range in host properties; Perley et al. 2016; Schulze et al. 2021).

In recent years, the Zwicky Transient Facility (ZTF; Graham et al. 2019; Bellm et al. 2019a) has detected a multitude of transients due to its moderately high-cadence and untargeted mapping of the entire northern sky down to 20.5 mag. The SNe observed by the ZTF collaboration in its first phase (2018 March – 2020 November) include sufficient numbers of SLSNe II to examine this subclass in greater quantity than previously done and to shed more light on the source of its often-extreme luminosity and ambiguous power source. To that end, in this paper, we present a sample of 14 SLSNe II from ZTF's phase I with broad Balmer lines but without strong narrow emission lines, examine their properties and fit their light curves using semi-analytical models of ^{56}Ni decay, magnetar spin-down and CSI.

We describe the sample and the ZTF survey itself in Section 2. We examine the spectroscopic evolution of the sample events in Section 3 and their light curves in Section 4, while comparing them to the objects in Inserra et al. (2018). We describe the light-curve modelling process and its results in Section 5, and examine the host galaxies of our sample in Section 6. We discuss our findings and possible power sources in Section 7, and present our conclusions in Section 8. Throughout this paper, magnitudes are in the AB system (Oke & Gunn 1983), and ΛCDM cosmological parameters are assumed to be $H_0 = 69.6$ km s^{-1} Mpc^{-1}, $\Omega_M = 0.286$, and $\Omega_\Lambda = 0.714$ (Bennett et al. 2014).

2 SAMPLE AND DATA REDUCTION

In the ZTF Northern Sky Public Survey (Bellm et al. 2019b) of ZTF, all fields with centre declination $\delta \geq -31^\circ$ and Galactic latitude $|\,b\,| > 7^\circ$ (i.e. $\sim$23 675 deg^2) are covered every three nights. This is roughly the entire Northern sky accessible from Palomar. Our target selection process is briefly described below. For more details, see Chen et al. (2022a).

A filter algorithm selects promising SLSN candidates from among ZTF alerts, which are then visually examined by human scanners. The filter excludes moving targets, stars, Galactic-plane targets, and bogus alerts. The filter also prefers faint, blue host galaxies and long rise times in order to minimize non-SLSN contamination. Nearly all candidates ($\geq$95 per cent) brighter than 18.5 mag are classified by the ZTF Bright Transient Survey (BTS; Fremling et al. 2020). The rest, if not already classified on the Transient Name Server,[1] were classified by the ZTF SLSN team and followed up.

Instruments used to observe the spectra in this paper were the Spectral Energy Distribution Machine (SEDM; Blagorodnova et al. 2018) and the Double Beam Spectrograph (DBSP; Oke & Gunn 1982) on the Palomar 60 inch (P60) and 200 inch (P200) telescope, respectively; the Low-Resolution Imaging Spectrometer (LRIS; Oke et al. 1995) on the Keck I telescope; the Alhambra Faint Object Spectrograph and Camera (ALFOSC) on the 2.56m Nordic Optical Telescope (NOT); the Intermediate-dispersion Spectrograph and Imaging System (ISIS) on the 4.2m William Herschel Telescope

[1] https://www.wis-tns.org/

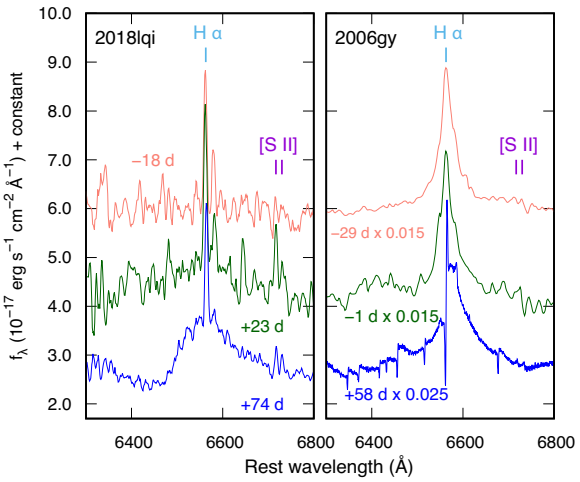

Figure 1. H α profile of SN 2018lqi at different epochs (left), compared to the profile in the superluminous Type IIn SN 2006gy (right; Smith et al. 2010). A broad component is clearly visible, but the unresolved narrow component is attributable to the host galaxy. A Type IIn profile, on the other hand, consists of a narrow core with Lorentzian wings.

(WHT); and the SPectrograph for the Rapid Acquisition of Transients (SPRAT) on the 2m robotic Liverpool Telescope (LT; Steele et al. 2004). The log of spectroscopic observations used here is available as supplementary material. A sample of the log is presented in Table A1.

The ZTF phase I ran from 2018 March 17 to 2020 November 30. During this period, a total of 63 SNe were discovered by the survey and classified as SLSNe II (note that this classification includes SLSNe IIn). The ZTF phase I also includes six events classified 'SLSNe I.5'; i.e. brighter than −20 mag and showing early spectroscopic similarity to SLSNe I, or simply lacking hydrogen lines until later during the photospheric phase. We define our sample as follows:

(i) Classified on the GROWTH Marshal (Kasliwal et al. 2019) as either SLSN I.5 or SLSN II, i.e. including hydrogen Balmer lines and brighter than −20 mag before *K*-correction (a total of 69 SNe);

(ii) Exhibiting a broad H α emission line – full-width half maximum (FWHM) of the broad component $\geq$5000 km s^{-1} – in at least one spectrum (20 SNe out of 69);

(iii) Lacking a typical Type IIn H α profile (i.e. a multicomponent profile with a narrow component from the SN) past the light-curve peak (14 SNe out of 20). Narrow features that disappear after the peak were ignored, as CSI lines are seen in many very early spectra of normal SNe II (Khazov et al. 2016; Bruch et al. 2021).

These criteria are based on the spectra from ALFOSC, DBSP, or LRIS, as very low-resolution spectra cannot reliably be used to detect narrow emission lines. Most objects in the sample show weak narrow emission lines that seem to originate in the host galaxy. Changing line ratios between H α and [O III] $\lambda\lambda$4959, 5007 and [S II] $\lambda\lambda$6717, 6730, or clearly Lorentzian profiles of the narrow Balmer line(s), imply an origin in the SN itself; otherwise an origin in the host galaxy is possible and we include the SN in our sample. The profiles of the narrow components are relatively weak, unresolved, and (when applicable) similar to the [O III] or [S II] profiles. As an example of a target with such behaviour, we show the H α profile of SN 2018lqi and its evolution in Fig. 1. We note that for SN 2018jkq, we only have a late-time (+170 d) spectrum with the broad H α emission, but both its early and late spectra strongly resemble other SNe in this sample.

The final sample of 14 SLSNe and their basic properties are listed in Table 1. The redshifts of the objects range from 0.057 to 0.403. The quality of the follow up varies widely, in terms of both spectroscopic cadence and the number of photometric filters used. As such, the narrow lines in two SLSNe IIn in ZTF are unresolved and may be from the host, and only early spectra exist – these SNe may have developed broad lines at a later epoch, but are not included. We also do not include objects where only pre-peak spectra exist and the narrow SN lines could in principle be replaced by broad lines at a later epoch – of these there are 12.

The majority of the *gri*-band photometry in our study is from the ZTF Observing System (Dekany et al. 2020) on the 48-inch Samuel Oschin Telescope in Palomar. This includes data from the public survey with a 3-d cadence and the ZTF partnership and Caltech surveys with a faster cadence ($\leq$2 d) over smaller areas (Bellm et al. 2019a). Additional photometry was obtained using SEDM and the optical imager (IO:O) on the LT. The ZTF data reduction and pipelines are managed by the Infrared Processing and Analysis Center (IPAC) at Caltech, as described by Masci et al. (2019). We have also obtained photometry, including upper limits, from the IPAC-forced photometry service.[2] The IPAC photometry makes use of the ZOGY algorithm (Zackay, Ofek & Gal-Yam 2016) for subtraction of reference images. The SEDM imaging data were processed using point-spread function photometry, and the magnitudes were calibrated against either SDSS or Pan-STARRS1 reference images, using FPIPE (Fremling et al. 2016). LT data were processed by a similar custom-built software (Taggart 2020). ZTF and LT *griz* magnitudes are calibrated to the Pan-STARRS1 photometric system and *u*-band data to the SDSS system. We include a table of all photometry used in this study as supplementary material; a sample of this table is presented in Table A2.

Reductions of P200/DBSP spectra were carried out using two pieces of software, PYRAF-DBSP (Bellm & Sesar 2016) as well as a newer PYTHON pipeline, DBSP_DRP (Roberson, Fremling & Kasliwal 2022), based on PYPEIT (Prochaska et al. 2020). Keck/LRIS data reduction used the custom-written, publicly available IDL-based software, LPIPE (Perley 2019). ALFOSC and ISIS spectra were reduced using standard procedures in IRAF (Tody 1986). SPRAT spectra were reduced by the automated LT pipeline (Barnsley, Smith & Steele 2012). SEDM spectra were processed by the PYTHON-based PYSEDM pipeline (Rigault et al. 2019); we note that the extracted spectra contain host galaxy light. All spectra presented in this paper will be available on WISEREP[3] (Yaron & Gal-Yam 2012).

Swift/UVOT data (for 8 of the 14 SNe) were retrieved from the NASA Swift Data Archive[4] and processed using the UVOT data analysis software HEASOFT 6.19.[5] The count rates were obtained from the images using the *Swift* tool `uvotsource`, using a circular 3 arcsec-radius region. The background was estimated using a significantly larger region close to the SN position. Counts were converted to magnitudes using the UVOT photometric zero-points (Breeveld et al. 2011a) and calibration files from 2020 September. Any host galaxies significantly contributing to the measured photometry[6] (based on visual inspection of *Swift* and *GALEX* images of the SN and its location) were subtracted from the *Swift* data using template images taken in late 2021. We also checked for *Swift* X-Ray Telescope (XRT)

[2] http://web.ipac.caltech.edu/staff/fmasci/ztf/forcedphot.pdf
[3] https://www.wiserep.org/
[4] https://heasarc.gsfc.nasa.gov/cgi-bin/W3Browse/swift.pl
[5] https://heasarc.gsfc.nasa.gov/
[6] This applies to SNe 2019cqc, 2019xfs, 2020jhm, and 2020yue.

Table 1. Properties of the SLSNe in our sample.

ZTF name	IAU name	RA (J2000, h:m:s)	Dec. (J2000, deg:m:s)	z	$A_{V,\,\mathrm{Gal}}$ (mag)	Classification
ZTF18acsxwdi	SN 2018jkq	01:09:31.53	+29:19:52.7	0.119	0.166	SLSN II
ZTF19aalvdeu	SN 2019kwr	13:22:12.35	+49:54:52.7	0.202	0.035	SLSN II
ZTF19aamrais	SN 2019cqc	18:21:43.05	+30:59:33.5	0.117	0.323	SLSN II
ZTF19aavakzo	SN 2019gsp	22:10:04.24	+23:28:38.5	0.171	0.231	SLSN II
ZTF19abxequc	SN 2019xfs	19:10:04.90	+32:20:41.4	0.116	0.513	SLSN II
ZTF19abxgmzr	SN 2019pud	21:12:55.00	−16:38:07.1	0.114	0.199	SLSN I.5
ZTF19acblhej	SN 2018lqi	02:18:21.94	−25:54:24.5	0.202	0.032	SLSN II
ZTF19ackiwff	SN 2019aanx	07:29:59.99	+13:05:43.2	0.403	0.235	SLSN II
ZTF19ackzvdp	SN 2019uba	02:23:28.74	−01:58:59.0	0.304	0.074	SLSN II
ZTF19adcfsoc	SN 2019zcr	12:58:42.92	+15:12:42.1	0.260	0.063	SLSN I.5
ZTF20aajvyja	SN 2020bfe	17:57:50.69	+33:47:48.1	0.099	0.120	SLSN II
ZTF20aatqene	SN 2020hgr	14:16:26.51	+70:24:48.8	0.126	0.042	SLSN II
ZTF20aayprqz	SN 2020jhm	15:33:02.28	+67:54:48.4	0.057	0.088	SLSN I.5
ZTF20acnznms	SN 2020yue	11:00:00.32	+21:06:45.8	0.204	0.054	SLSN II

detections: no SN in the sample was detected in 0.2–10 keV XRT observations over a range of epochs from before the optical peak to >2 yr after the peak. We list the XRT upper limits in Table B1 in Appendix B, where we also describe the process of estimating the limits.

3 SPECTROSCOPIC EVOLUTION

3.1 Common spectral features of the sample

Our sample has been selected so that the only common factors are the luminosity and the presence of broad Balmer emission lines without strong narrow lines. A large fraction of the sample none the less exhibits a broadly similar spectral evolution: an early phase with blue and nearly featureless spectra at and around the light-curve peak, followed by the appearance of broad Balmer emission, sometimes with a P Cygni profile. The sequence is shown in Fig. 2 for each object in the sample. All phases below refer to the light-curve peak in the rest-frame g band (see Section 4). The broad emission lines are often contemporaneous with the appearance of absorption lines of Na I + He I, Fe II, Sc II and emission from Mg I] and Ca II. The lines and their velocities (5000–15 000 km s^{-1}) in most of our objects resemble Type II SNe in general, with weaker Hα absorption than is typical for SNe II-P but similar to SNe II-L. The prototypical SN 2008es has also been shown to bear some similarity to the luminous Type II-L SN 1979C (Gezari et al. 2009; Miller et al. 2009), albeit with a delayed spectroscopic evolution, as did CSS121015 (Benetti et al. 2014) and PS15br (Inserra et al. 2018).

A strong broad Hα line mostly does not develop until weeks after maximum light, but a weak emission is seen in the early spectra of some SNe in the sample. Late-emerging Balmer lines are often seen in SNe II-L (e.g. Fassia et al. 2001; Kangas et al. 2016; Terreran et al. 2016), and also seen in three of the four previously observed SLSNe II: SN 2008es, CSS121015, and PS15br. However, this is not ubiquitous: SNe 2020hgr and 2020yue develop a strong broad emission line before the peak, as did SN 2013hx (Inserra et al. 2018) and the normal Type II-L SN 1980K (Uomoto & Kirshner 1986).

We have late-time (>200 d) spectra available for 6 of the 14 SNe in our sample.[7] Additionally, for SN 2018jkq, we have a +170 d spectrum. The latest-phase spectra of these SNe are shown in Fig. 3, together with a comparable-epoch spectrum of PS15br (Inserra et al. 2018) for comparison. The spectrum is generally dominated by a strong, broad Hα emission line (FWHM $\gtrsim$ 5000 km s^{-1}), accompanied by a weaker Hβ line and little else. When its wavelength is covered, we see the Ca II infrared triplet except in the case of SN 2019pud, where the comparatively weak blue wing of the Hα profile is also exceptional.

Similarly to PS15br and SN 2013hx (Inserra et al. 2018), we see no clear [O I] λλ6300, 6364 emission, which is typically strong in normal SNe II (e.g. Terreran et al. 2016; Dessart & Hillier 2020) and SLSNe I (e.g. Chen et al. 2015; Jerkstrand et al. 2017) at similar epochs. The typically similarly strong [Ca II] λλ7291, 7323 doublet is weak or non-existent as well, only clearly seen in SN 2020hgr. There is a difference as well: PS15br and SN 2013hx evolved to show a multicomponent Hα profile at $\gtrsim$230 d, suggesting late-time CSI. In our spectra, the emission profile typically only shows one component. A possible narrower component is visible in SN 2019pud at $\gtrsim$300 d and SN 2020bfe at $\gtrsim$190 d, but the multicomponent profile is unclear compared to Inserra et al. (2018).

3.2 Spectroscopic subgroups

There are some indications of subgroups within the sample. Three SNe in the sample are quite similar to SN 2008es in terms of their photospheric-phase spectra; these are SNe 2019aanx, 2019uba, and 2019zcr, and we henceforth refer to these SNe as '08es-like'. The same SNe are also similar to SN 2008es photometrically (see Section 4). This resemblance is demonstrated in Fig. 4. Not all features of the SN 2008es spectra are replicated, but this is at least partially due to the noisy spectra of these distant (z = 0.26 to z = 0.40) SNe. We do, however, see similar shapes (broad, symmetric emission with no P Cygni absorption) and widths (6000–8000 km s^{-1}) in their Hα profiles, and weak absorption lines compared to the rest of the sample, at the same phases. The broad component shows a possibly Lorentzian profile, albeit without the strong narrow core typical for SNe IIn. An intermediate or emerging/weak broad emission component is seen around peak, similarly to PS15br (Inserra et al. 2018). Signs of a 'bump' feature are also seen blueward of ∼5700 Å, albeit quite weak in the available spectra of SN 2019uba. Such a feature is associated with a pseudo-continuum comprised of a forest of blended iron lines, often seen in interacting Type IIn and Ibn SNe (e.g. Turatto et al. 1993; Karamehmetoglu et al. 2021; Kool et al.

[7]This does not include late-time spectra (those of SNe 2019kwr, 2018lqi, and 2020jhm) where only host galaxy lines are seen.

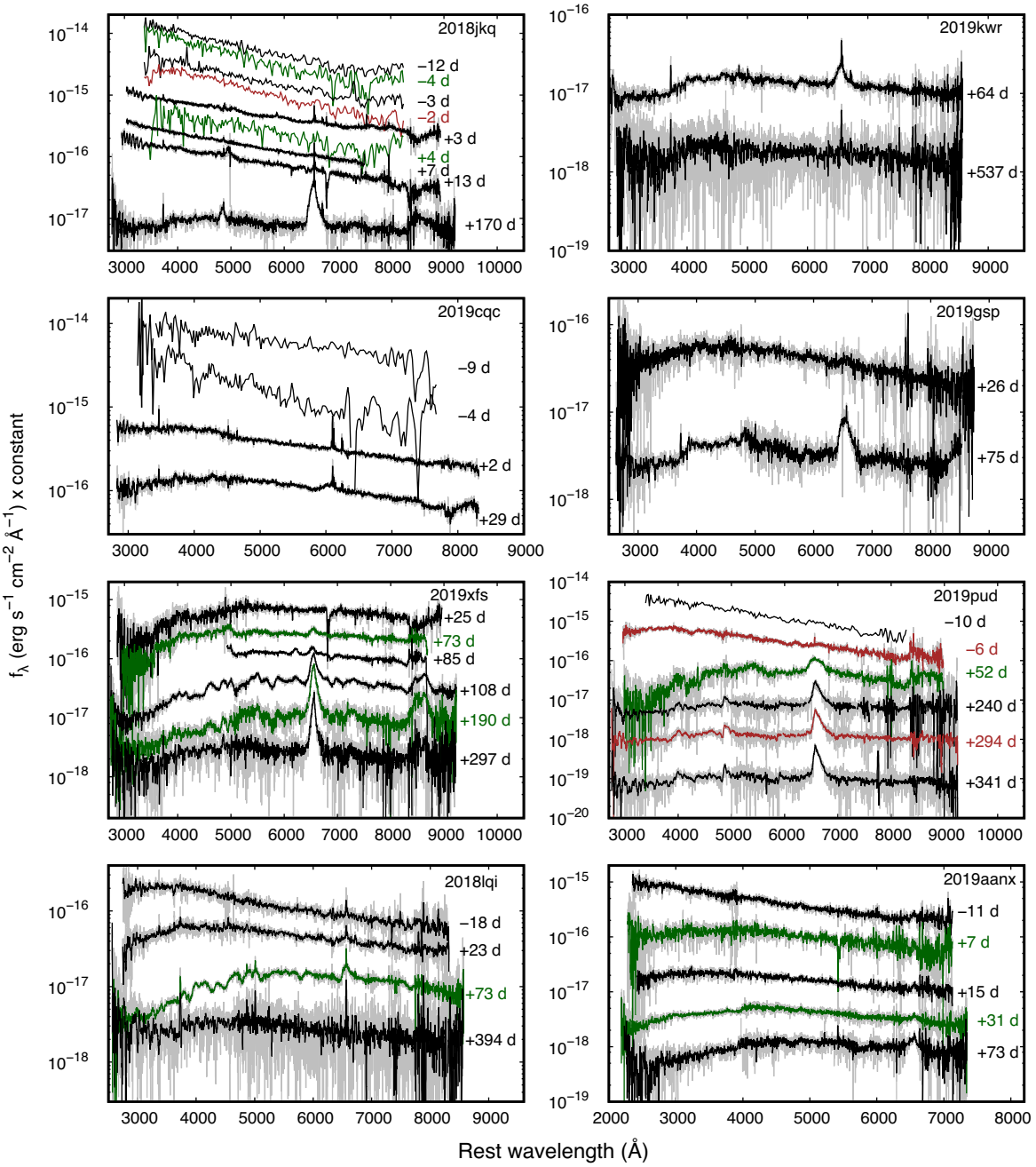

Figure 2. Spectral sequences of the SNe in our sample. The colours of overlapping spectra are different for clarity. All epochs refer to rest-frame *g*-band light-curve peaks. Savitzky–Golay smoothing has been applied; the original spectra are plotted in grey.

2021). The symmetric shape of the Hα emission profile continues until late times.

A majority of our sample, however, spectroscopically resembles typical SNe II more than SN 2008es. These are SNe 2019kwr, 2019cqc, 2019gsp, 2019xfs, 2018lqi, 2020bfe, 2020hgr, and 2020yue. We show a comparison between SNe 1999em, 1979C, and 1998S and these SNe (with the exception of SN 2020yue as it lacks spectra in the shown phases) in Fig. 5. We also include SN 2019pud in this figure despite its early-time peculiarity (see below). Features seen in these events include a selection of absorption and P Cygni lines typical to Type II SNe (O I, Na I + He I, Sc II, Fe II, and Mg I]), with relatively shallow or often undetected absorption in Hα. These features are typical for Type II-L spectra in particular. The widths of the absorption lines extend to roughly $-10\,000$ km s^{-1} in the phases ($>+50$ d) where they are clearly visible. We only have early spectra of SN 2020yue, which resemble those of a young SN II-P with strong, broad P Cygni profiles for the Balmer lines. This is atypical for our sample, where early spectra tend to be featureless. For SN 2019cqc our latest-phase spectrum is at + 29 d, which shows a shallow but very broad P Cygni feature (extending up to $\sim-20\,000$ km s^{-1}) in Hα and in the Ca II near-infrared (NIR) triplet. These lines are likely still in the process of emerging, as the peak-phase spectrum is featureless.

The last subgroup consists of three SNe with more peculiar spectra or uncertain evolution. SN 2018jkq was not spectroscopically

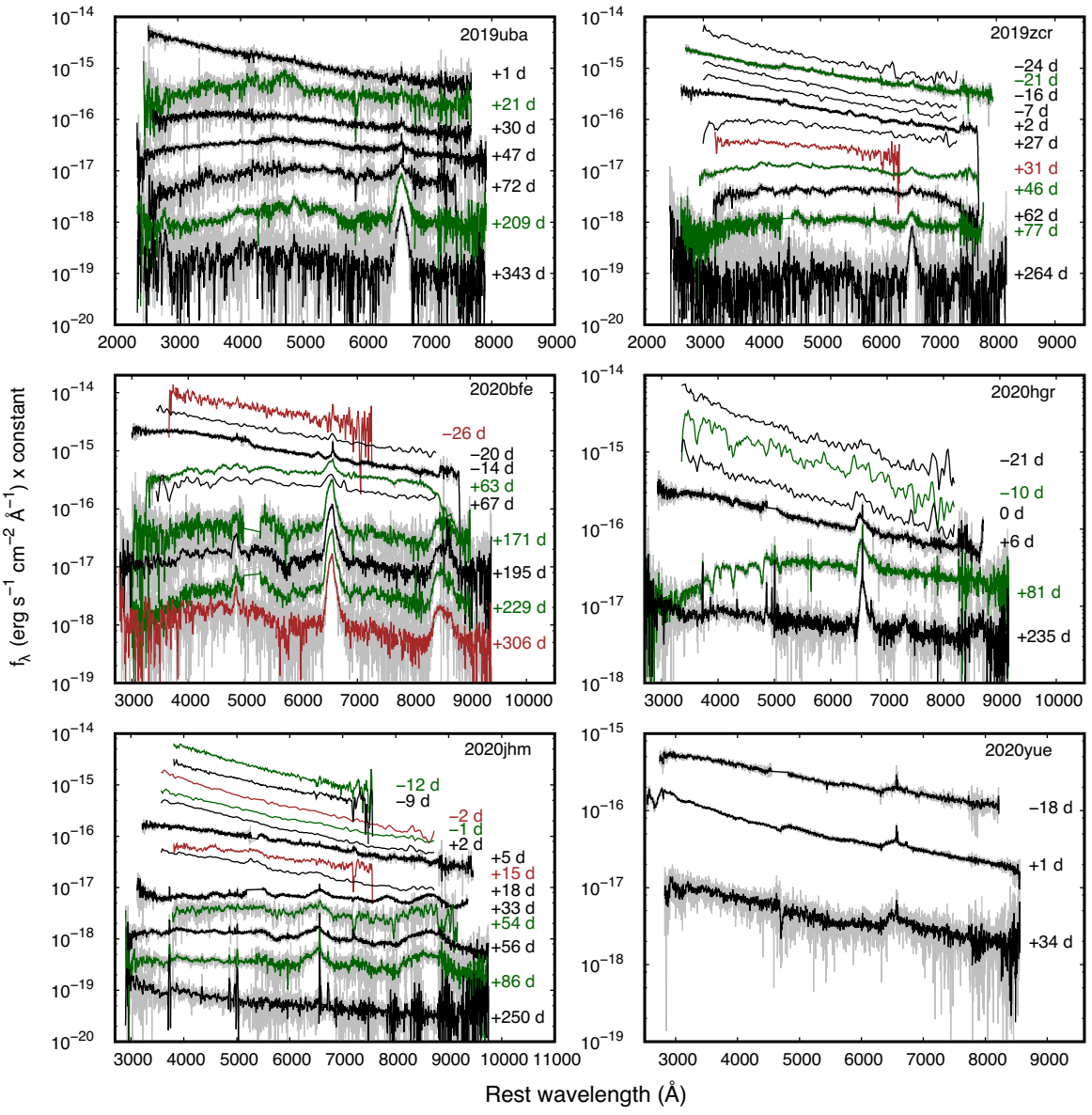

Figure 2. *– continued*

observed between the peak (featureless apart from weak, narrow Balmer lines) and the late-phase, but the spectrum at + 170 d exhibits broad (FWHM ∼5500 km s^{-1}) emission of Hα, Hβ, and Ca II very similarly to several other SNe in our sample. SN 2019pud eventually starts to resemble SN 1979C, but early on shows a broad absorption feature at ∼4250 Å, atypical for Type II SNe. Multiple lines could be responsible for this feature, such as those of Fe III or O II; we cannot definitively identify this line. Finally, SN 2020jhm is spectroscopically unique within the sample. Its early spectra are blue and featureless, but around + 30 d it develops strong, broad emission lines of Hα, the Ca II NIR triplet and O I λ7774. The O I emission then rapidly weakens, while the other emission lines eventually extend to ∼−18 000 km s^{-1}. The pseudo-continuum of iron lines around 5600 Å is also seen in this SN. Apart from the absence of narrow emission lines, the spectrum resembles SN 1988Z (Turatto et al. 1993), albeit at an earlier phase; see Fig. 6. SNe 2019pud and 2020jhm also exhibit peculiar early light curves (see Section 4).

4 LIGHT CURVES

4.1 Peak fits and absolute magnitudes

We have performed numerical interpolation of each light curve using a Gaussian process (GP) regression algorithm (Rasmussen & Williams 2006) to obtain peak magnitudes and epochs. We used the PYTHON-based GEORGE package (Ambikasaran et al. 2015), which implements various different kernel functions. Matérn kernels with ν parameter of 3/2 or 5/2 were used. The uncertainty in peak epoch is estimated as the time range when the GP light curve is brighter than the 1σ lower bound on the peak brightness.

K-corrections (Hogg et al. 2002) were performed using the $-2.5\log(1+z)$ approximation. For the SNe where we have a spectrum close to the light-curve peak (7 out of 14 events), we have also determined the spectroscopic *K*-correction using the SNAKE code (Inserra et al. 2018). As seen in Fig. 7, for these SNe the approximation is good to within ∼0.1 mag. A similar trend

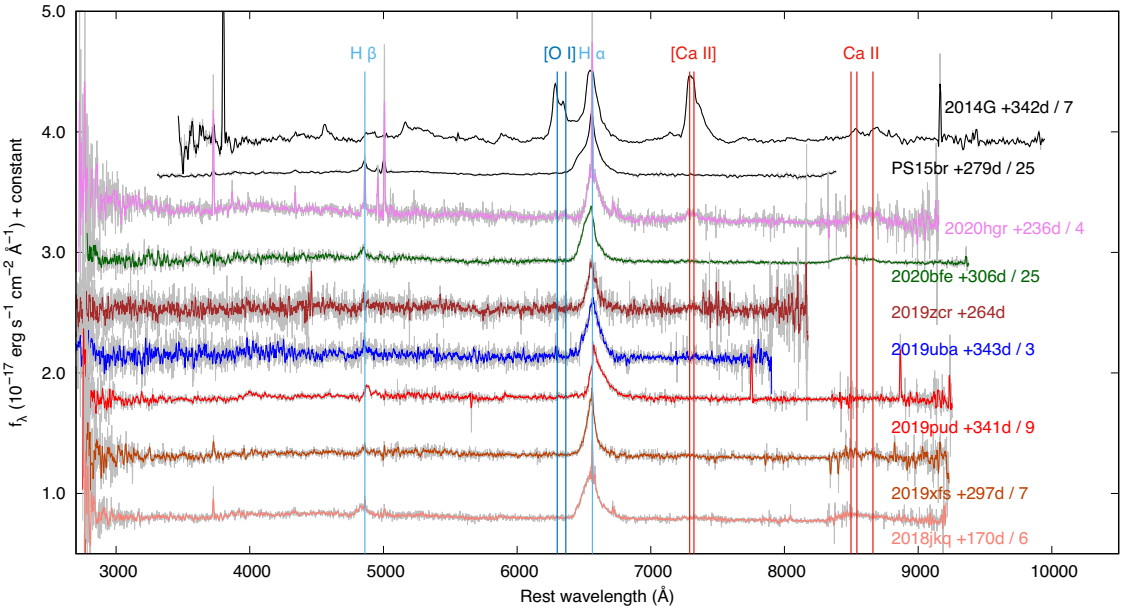

Figure 3. Comparison between late-time spectra of the Type II-L SN 2014G (Terreran et al. 2016), the SLSN II PS15br (Inserra et al. 2018), and the seven SNe in our sample with available spectra in this phase, corrected for Galactic extinction.

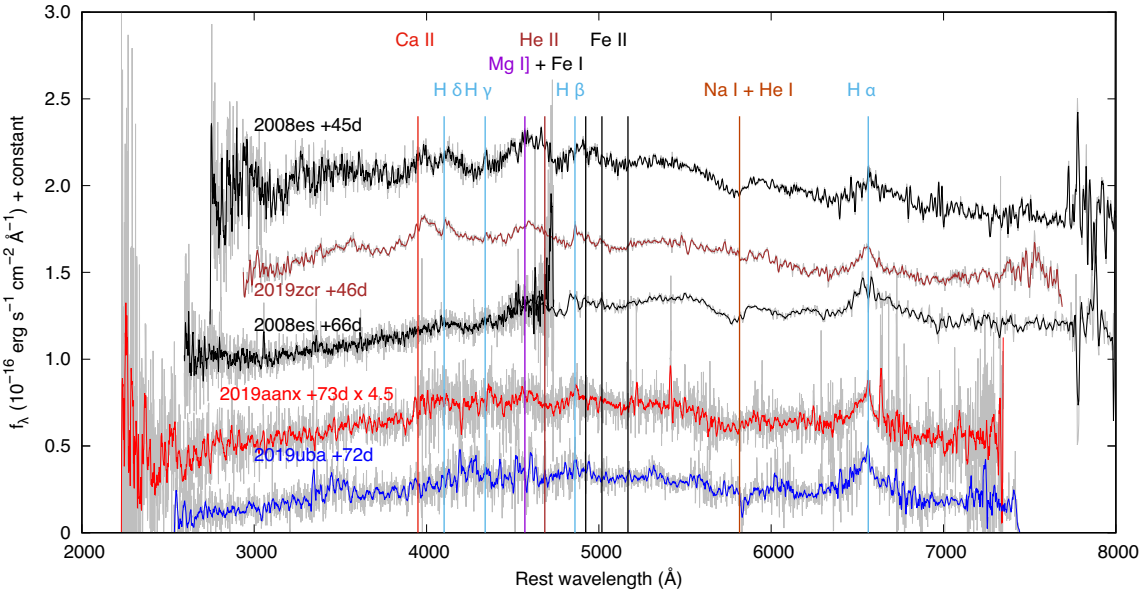

Figure 4. Comparison between the spectra of SN 2008es (Gezari et al. 2009; Miller et al. 2009) and the three similar SNe in our sample, corrected for Galactic extinction.

was shown for SLSNe I by Chen et al. (2022a). Spectroscopic *K*-corrections are not possible for the majority of epochs, and we have thus, for the sake of uniformity, used the approximation for all photometric points. Thus we have obtained the absolute light curves of each SN using

$$M_{\rm R} = m_{\rm O} - \mu - A_{\rm O,Gal} + 2.5\log(1+z), \quad (1)$$

where R stands for the rest-frame filter, O is the observed filter, μ is the distance modulus, and $A_{\rm O,\,Gal}$ is the Milky Way extinction (Schlafly & Finkbeiner 2011) in filter O determined using the Cardelli, Clayton & Mathis (1989) law. For redshifts $z < 0.17$ (7 out of 14 events), filters O and R are the same. Otherwise R is the filter with the closest effective wavelength to the redshift-corrected effective wavelength of O, in the sequence of UVW2, UVM2, UVW1, *u*, *g*, *r*, *i*, and *z*.

The peak parameters, rise times from half-maximum, and decline parameters of our SNe are listed in Table 2. Here, we use both Δg_{50}, i.e. the decline from the *g*-band light-curve peak in 50 rest-frame days, and s_2, the decline rate during the late photospheric phase (Anderson et al. 2014). We show the absolute rest-frame *g* band light curves of all sample SNe together in Fig. 8. The individual multiband GP light curve of each SN is shown in Fig. 9 (SNe with GP fits in at least four bands) and Fig. 10 (the rest) for the filters where a GP fit is feasible. We have used the GP fits to obtain the rest-frame $g - r$ colours when possible; we show these in Fig. 11.

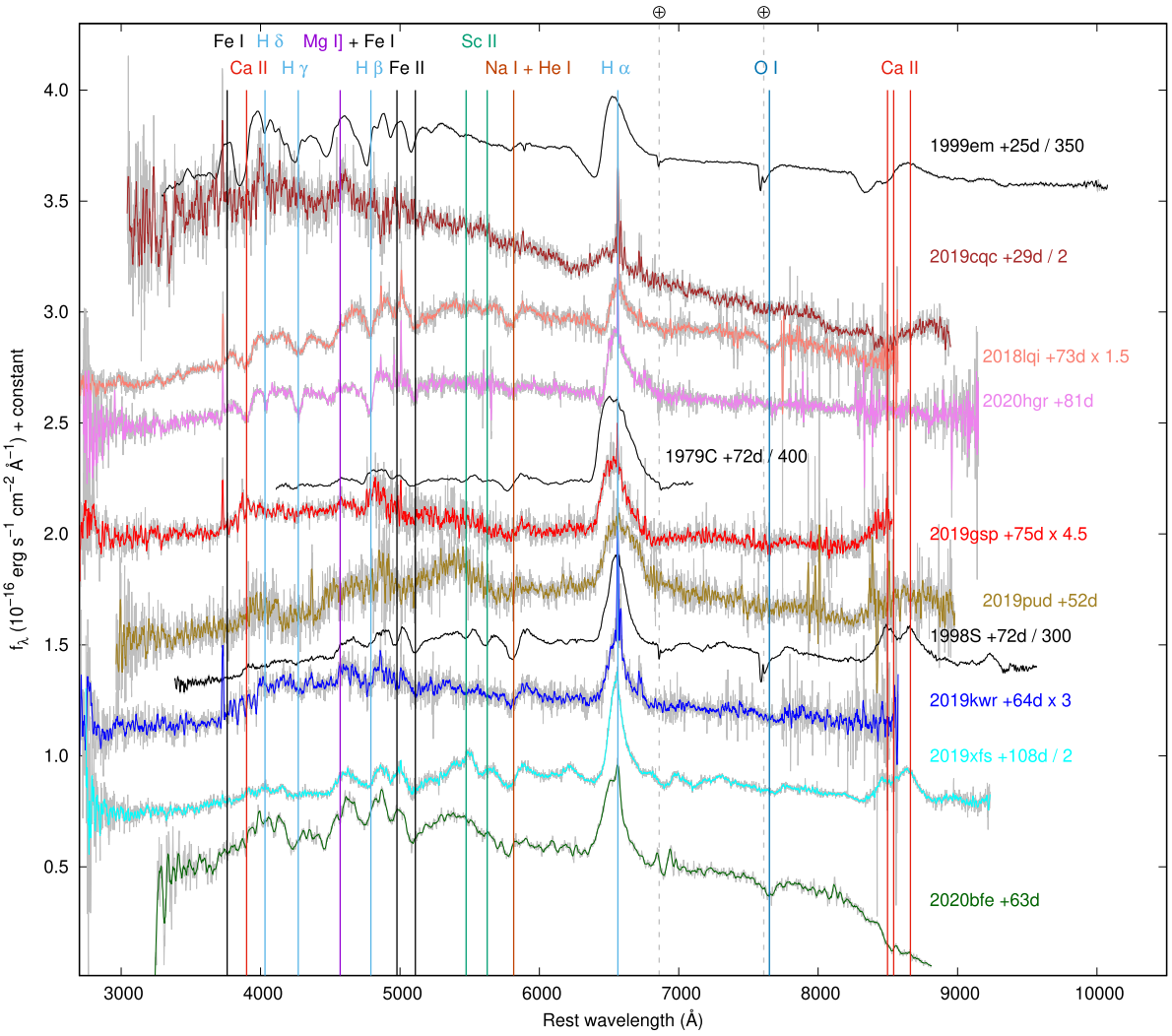

Figure 5. Comparison between the spectra of normal Type II-P SN 1999em (Elmhamdi et al. 2003), the luminous Type II-L SNe 1979C (Branch, Nomoto & Filippenko 1991) and 1998S (Fassia et al. 2001), and similar SNe in our sample, corrected for Galactic extinction. Telluric lines (⊕) have been marked for SNe 1999em, 1979C, and 1998S; these have been removed from the ZTF spectra.

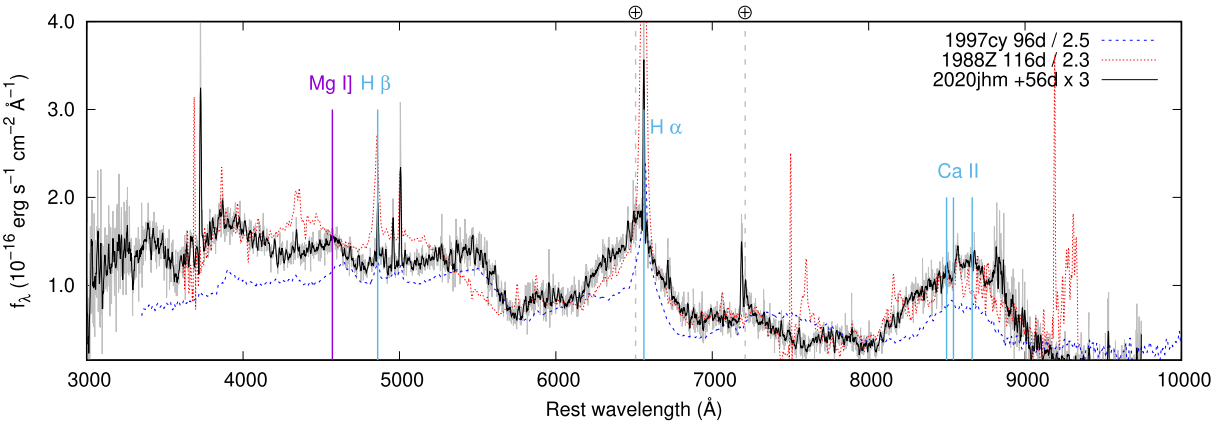

Figure 6. Comparison between the spectra of SN 2020jhm (black solid) and interacting SNe 1988Z (red dotted, Type IIn; Turatto et al. 1993) and 1997cy (blue dashed, Type IIn or Ia-CSM; Turatto et al. 2000; Hamuy et al. 2003), corrected for Galactic extinction. Similarities can be seen between all three events, although the evolution of SN 2020jhm is somewhat faster. Dates for SNe 1988Z and 1997cy refer to the discovery date. Telluric features (⊕) are marked.

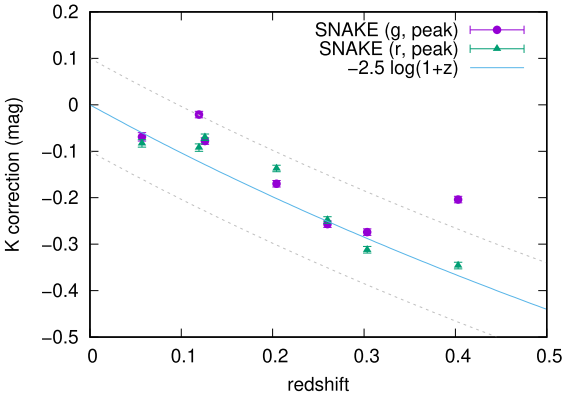

Figure 7. Approximate K-corrections using $-2.5\log(1+z)$ (line) compared to the values determined using SNAKE (Inserra et al. 2018) from spectra close to peak for the SNe where this was possible (points). The dashed lines correspond to ± 0.1 mag and contain most of the variation.

Any host galaxy extinction has not been accounted for. We do not detect narrow Na I D absorption in any of our spectra, indicating that host galaxy extinction is moderate at worst. We note that the peak-phase rest-frame $g - r$ colours within the sample vary from roughly 0.2 to -0.2 mag (see below and Fig. 11), which may indicate differences in host galaxy extinction. There is, however, considerable diversity within the sample in terms of light curves and spectra, and intrinsic colour differences are likely to exist. Therefore, we have not attempted to use colour differences to determine host extinction.

4.2 Photometric properties

From Fig. 8, it is clear that the light curves of the class formed by our sample and the SLSNe II previously studied by Inserra et al. (2018) are somewhat heterogeneous. Most of the events are clustered between peak g-band magnitudes of roughly -20 and -21 mag. This group includes a range of decline time-scales, but most of the light curves decline at a similar rate, between 1.5 and 2 mag (100 d)$^{-1}$. This also applies to the second group within our sample, at peak magnitudes brighter than -21 mag – but not to SN 2013hx and SN 2008es, which decline at $\sim$4 mag (100 d)$^{-1}$. There is also considerable variation in rise times from half-maximum (Table 2), which range from 10 to 20 d (SNe 2018jkq, 2019pud, and 2020jhm) to $\sim$55 d (SN 2019aanx) in the rest-frame, mostly clustering around 30–50 d. This heterogeneity is therefore not only seen between, but also within, the spectroscopic subgroups.

Some heterogeneity is also seen in the colour evolution. The fast-evolving events, SN 2019pud and SN 2020jhm, stand out in Fig. 11. From $\sim$20 d onwards (rest-frame), they redden quickly from $g - r \approx -0.2$ mag at the peak to $g - r \sim 0.6$ mag, then their evolution flattens or even moves back towards the blue from $\sim$35 d onwards. The slowest-evolving SN in the sample, SN 2020hgr, reddens until at least 110 d and reaches a colour of $g - r \gtrsim 0.8$ mag. The rest of the sample tends to redden slower, reaching $g - r \sim 0.5$ mag around 100 d. The colours at the peak lie roughly between -0.2 and 0.1 mag. Intrinsic colour differences are likely considering the variety in other features, but if this range was entirely due to host extinction, a difference of 0.3 mag in $g - r$ colour would correspond to $A_V \lesssim 1$ mag (Cardelli et al. 1989).

To illustrate the range of light-curve behaviour, we show the decline rate (see Table 2) as a function of the peak magnitude in Fig. 12. Here, we measure the former with the quantity Δg_{50}, determined using GP interpolation. We have also measured the decline rates quantified as s_2 (Anderson et al. 2014) for our sample. This is defined in normal SNe II as the decline rate in the plateau or bump phase, following an initial, steeper decay s_1. In most of our sample, we cannot clearly separate s_1 and s_2, in which case we have measured s_2 after the light curve has clearly turned over from the peak.

In the top panel, we also include the SLSNe II in Inserra et al. (2018), CSS121015 (Benetti et al. 2014) and the prototypical SLSN II, SN 2008es (Gezari et al. 2009; Miller et al. 2009). We also include various SNe of different types and separate our sample events into

Table 2. Rest-frame g-band peak absolute magnitudes, peak epochs, rise times from half-maximum ($t_{\rm rise,\,0.5}$), and decline parameters Δg_{50} and s_2 of our sample SNe based on GP fits using GEORGE (Ambikasaran et al. 2015). The peak magnitudes are de-reddened for Galactic extinction and K-corrected. The errors quoted here are solely based on the GP fits.

SN	Peak MJD (d)	Abs. g-band peak (mag)	$t_{\rm rise,\,0.5}$ (d, rest)	Δg_{50} (mag)	s_2 [mag (100 d)$^{-1}$]
SN 2018jkq	$58475.5^{+2.5}_{-2.7}$	-20.74 ± 0.04	$15.5^{+2.4}_{-2.5}$	0.70 ± 0.14	1.6 ± 0.3
SN 2019kwr	58589.0 ± 3.8	-20.25 ± 0.03	$32.7^{+3.4}_{-3.2}$	1.00 ± 0.05	2.7 ± 0.2
SN 2019cqc	$58595.2^{+4.1}_{-3.7}$	-20.21 ± 0.02	$27.7^{+3.8}_{-3.4}$	0.72 ± 0.04	1.3 ± 0.1
SN 2019gsp	58636.1 ± 6.7	-20.54 ± 0.03	15.9 ± 5.8^{a}	1.36 ± 0.06	4.5 ± 0.6
SN 2019xfs	$58809.6^{+6.4}_{-15.1}$	-20.97 ± 0.03	$55.3^{+5.8}_{-13.6}$	1.14 ± 0.50	2.6 ± 0.3
SN 2019pud	58754.6 ± 3.6	-20.96 ± 0.05	$13.7^{+3.3}_{-3.4}$	2.63 ± 0.12	3.2 ± 0.3
SN 2018lqi	$58783.7^{+13.1}_{-10.9}$	-20.57 ± 0.04	$30.3^{+11.0}_{-9.2}$	0.67 ± 0.22	2.3 ± 0.2
SN 2019aanx	$58828.4^{+1.0}_{-22.4}$	-21.92 ± 0.02	$46.0^{+0.8}_{-16.0}$	0.82 ± 0.10	2.1 ± 0.4
SN 2019uba	58810.2 ± 4.0	-21.70 ± 0.02	$>18.3^{b}$	0.81 ± 0.04	1.3 ± 0.3
SN 2019zcr	$58901.4^{+1.6}_{-7.8}$	-22.61 ± 0.07	$33.4^{+1.8}_{-6.5}$	0.61 ± 0.08	2.4 ± 0.2
SN 2020bfe	$58919.5^{+7.3}_{-6.3}$	-20.20 ± 0.02	$35.3^{+6.7}_{-5.8}$	0.44 ± 0.06	1.9 ± 0.2
SN 2020hgr	$58990.7^{+5.1}_{-4.2}$	-20.06 ± 0.01	$42.9^{+4.6}_{-3.8}$	0.55 ± 0.02	2.2 ± 0.2
SN 2020jhm	$58990.9^{+3.5}_{-0.7}$	-20.33 ± 0.03	$11.3^{+3.4}_{-0.8}$	2.95 ± 0.04	2.6 ± 0.4
SN 2020yue	$59193.3^{+8.1}_{-7.6}$	-21.26 ± 0.03	$>30.9^{b}$	0.68 ± 0.04	1.3 ± 0.2

[a]The rise of SN 2019gsp is only covered by the rest-frame B-band light curve, which is used here.
[b]The rises of SNe 2019uba and 2020yue are not fully covered by our observations, and a lower limit based on the first detection is given.

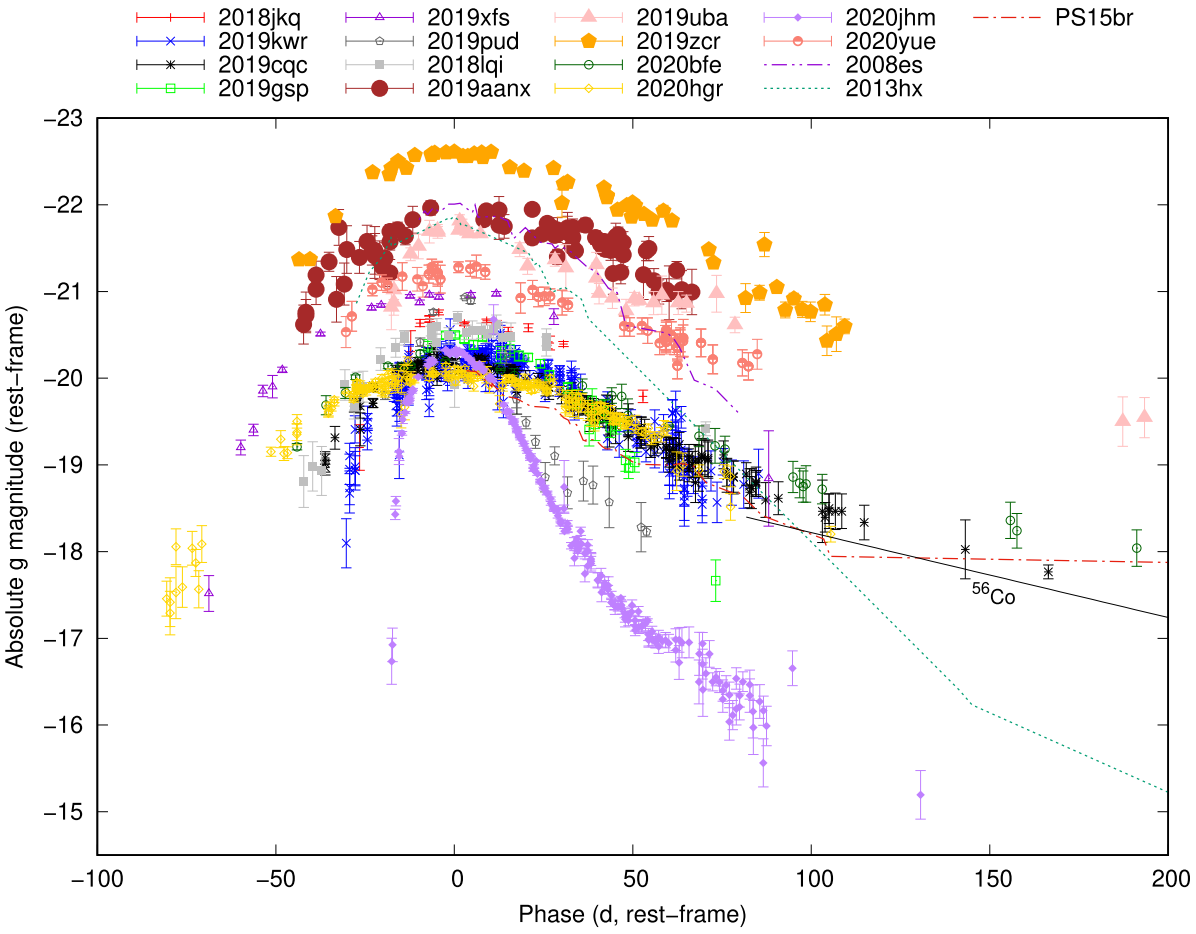

Figure 8. Absolute-magnitude light curves of our sample SNe in the rest-frame g band (points). We also show the previously studied SLSNe II: SN 2008es, SN 2013hx, and PS15br (lines; Gezari et al. 2009; Inserra et al. 2018). Large symbols correspond to the 08es-like SNe in our sample. The phase refers to rest-frame days after the light curve maximum. The heterogeneity of the SNe is apparent in terms of peak magnitude and decline rate.

groups based on spectroscopic similarities (see Section 3). Here, we consider CSS121015 and PS15br spectroscopically 08es-like, while the spectrum of SN 2013hx evolves to resemble normal SNe II (see fig. 2 of Inserra et al. 2018). It is apparent that the brightest SLSNe II are all 08es-like. The other SNe, most of which resemble normal Type II SNe more, tend to be fainter. However, PS15br is among the faintest in the sample and thus an outlier.

Most of our sample is located below $\Delta g_{50} \approx 1.5$ mag, as are the previously studied SLSNe II. There are two outliers: SNe 2019pud and 2020jhm (respectively, with Δg_{50} of 2.6 and 3.0 mag). In terms of s_2, these SNe are not outliers, implying that their early steep decline does not persist into late times. Both of these SNe were classified Type I.5, while the third SLSN I.5 in this sample, SN 2019zcr, is the brightest (peaking at -22.61 ± 0.07 mag) and among the slowest ($\Delta g_{50} \approx 0.6$ mag). Spectroscopically, the latter resembles SN 2008es, while the former two do not closely resemble either SN 2008es, normal SNe II, nor each other (see Section 3). Thus it is clear that the events classified as Type I.5 do not form a unified group; the classification of both fast-evolving outliers as Type I.5 may be a coincidence. The third SN in the 'other' group in Fig. 12, SN 2018jkq, is in this group due to a lack of spectra, not any observed difference in evolution. However, it is photometrically similar to the 'II-P/L-like' group.

Most of the light curves of this sample never exhibit a late time decline similar to ^{56}Co decay, i.e. 0.98 mag (100 d)$^{-1}$; however, it is possible that most of the observed light curves simply do not reach that phase. Three SNe, SN 2019cqc, SN 2019uba, and SN 2020bfe, have light curves extending to >150 d and do show a flattening decline. The rest-frame g-band decline rates at >100 d in these events are 1.01 ± 0.04, 0.10 ± 0.72, and 0.74 ± 0.04 mag (100 d)$^{-1}$, respectively; thus only SN 2019cqc is within 1σ of the ^{56}Co decay rate, while the large uncertainty of SN 2019uba puts it within 2σ. SN 2020bfe, meanwhile, declines too slowly for ^{56}Co decay, which can be caused by a CSM or magnetar power source still being dominant at late times.

4.3 Comparison to other events

The rise times from half-maximum within our sample can mostly be determined from the GP fit. The median rise time is $\tilde{t}_{\mathrm{rise},0.5} = 33 \pm 6$ d, and three SNe (SNe 2019xfs, 2019aanx, and 2020hgr) have $t_{\mathrm{rise},\,0.5} > 40$ d. This is not only much longer than is typical for Type II SNe (where the rise times from *explosion* have a 1σ range of 4–17 d; González-Gaitán et al. 2015), but also longer by a factor of $\gtrsim$2 than what was observed for the luminous Type II-L SN 1998S ($\sim$17 d from explosion; Fassia et al. 2000). SLSNe I, on the other hand, exhibit rise times similar to the SLSNe II (Chen et al. 2022a). The two peculiarly fast-declining SLSNe II, SN 2019pud and SN 2020jhm, are also fast to rise (rise times from explosion

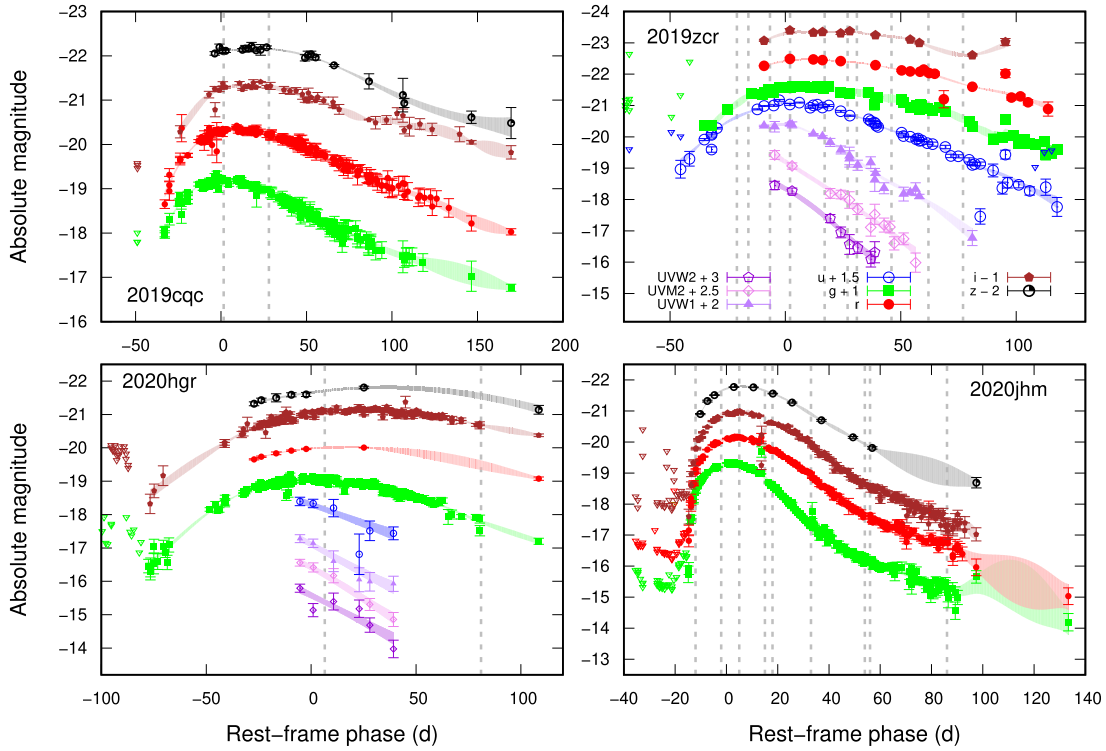

Figure 9. Our GP fits to the light curves of the four SNe in our sample with sufficient coverage in at least four bands. Large symbols correspond to an 08es-like SN. Vertical dashed lines correspond to the epochs of spectra.

are ∼20 and ∼17 d, respectively), and close to the range of non-superluminous SNe II.

Normal SNe II (including II-L) tend to exhibit a plateau or similar phase of flattening in their light curves (Anderson et al. 2014; Valenti et al. 2015). Only very few SNe II-L show a truly linear light curve after the diffusion peak, such as SN 2016gsd (Reynolds et al. 2020), which had a peak absolute magnitude of ∼−20 mag. Generally speaking, we do not observe the normal sequence of a clear plateau or bump phase, followed by a drop to a radioactive tail phase, in our sample SNe. It is possible that such a phase exists in SN 2019pud and SN 2019uba, but these features could also be undulations, similar to what is often seen in SLSNe I (Hosseinzadeh et al. 2022; Chen et al. 2022b). Undulation features in the light curve can be signs of CSI, but these are not observed in 08es-like events or luminous SNe II-L. Our light curves extend to beyond the typical plateau phases of ≲100 d (see e.g. Reynolds et al. 2020) in six cases; for the remaining five with no clear bumps (as shown in Fig. 10), it is possible that the bump or flattening phase occurred after our coverage ended.

The normal SNe II included in the sample of Anderson et al. (2014) show an increasing decline rate s_2 with brighter peak magnitude. However, we do not see any such – or opposite – trend in our sample (see Fig. 12): the s_2 rates are similar for all SNe studied here regardless of brightness, typically in the range of 1–4 mag (100 d)$^{-1}$. This is also the range of normal SNe II at peak magnitudes ≲−17.5 mag. While neither we nor Anderson et al. (2014) include SNe II between −19 and −20 mag in our samples, this suggests the s_2 trend flattens out after ∼−18 mag. We note, though, that s_2 normally refers to the plateau/bump phase that our sample generally does not exhibit.

This lack of a plateau or bump is not the only photometric difference to the luminous SN II-L group (Fig. 12), despite the spectroscopic similarity: they also tend to decline faster at early times than SLSNe II. The plateauless SN 2016gsd (Reynolds et al. 2020), on the other hand, approaches the decline rates seen in these samples as expressed with the Δg_{50} parameter. The fast-evolving SNe 2019pud and 2020jhm are the exceptions: these events show a decline and a colour evolution in the first 50 d comparable to or even faster than luminous SN II-L events (especially SN 2013fc; Kangas et al. 2016), but differ spectroscopically from these events, as opposed to the rest of the sample (see Section 3). All in all, while two luminous SNe II-L, SN 1979C (Panagia et al. 1980) and SN 2013fc (Kangas et al. 2016), fulfil our criteria as established in Section 2, our sample does not include any SNe that are *both* spectroscopically and photometrically similar to them.

We note that, in terms of light curves, there is considerable overlap between the ZTF SLSNe IIn, compiled from photometry publicly available through the BTS Sample Explorer[8] (Perley et al. 2020), and our sample. This applies especially to the II-P/II-L-like group in Fig. 12. Meanwhile, the SLSNe I show a wide range of photometric properties, also resulting in overlap, but our sample includes relatively fewer fast-declining events. The II-P/II-L-like SNe do not extend to the brightest peak magnitudes, while the bright 08es-like events only overlap with the edge of the SLSN I distribution. Nevertheless, as a whole, SLSNe II show more similarity to SLSNe I and especially to SLSNe IIn in their photometric evolution than to normal SNe II or luminous SNe II-L.

4.4 Ultraviolet excess

The spectral energy distributions (SEDs) of SLSNe I are affected by considerable line blanketing in the ultraviolet (UV) region, which

[8]https://sites.astro.caltech.edu/ztf/bts/explorer.php

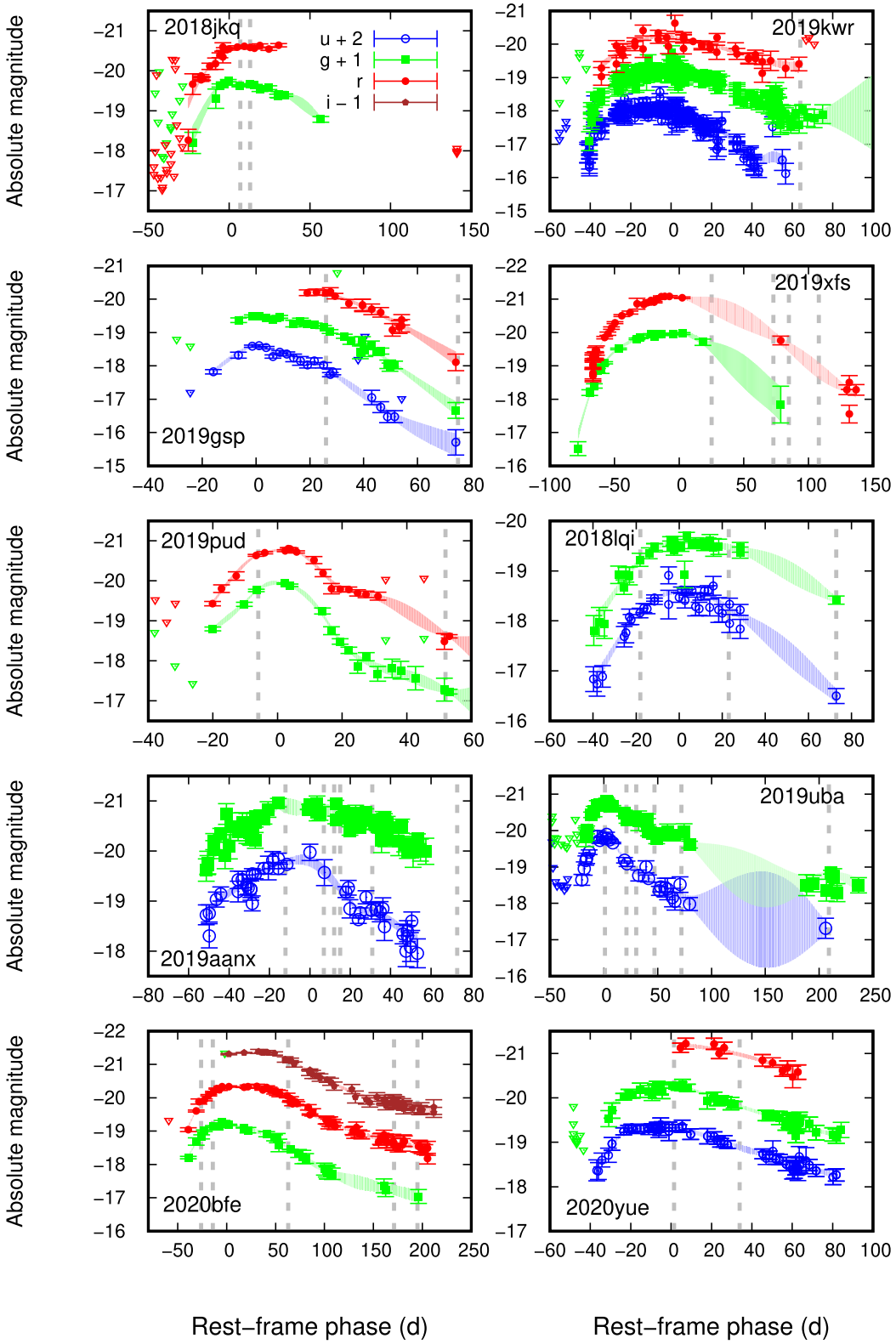

Figure 10. Our GP fits to the light curves of the 10 SNe in our sample with sufficient coverage in only two or three bands. Large symbols correspond to the 08es-like SNe. Vertical dashed lines correspond to the epochs of spectra.

is taken into account in the models that we employ in Section 5 (Nicholl, Guillochon & Berger 2017). In order to determine whether this affects our sample as well, we have performed blackbody fits on the six events where we have *Swift* UV photometry available. We show these fits in Fig. 13. Clearly, a simple blackbody is not a good description of four of these six SNe; but instead of a UV deficit caused by line blanketing, we see a UV *excess* that, especially in the observed UVW2 band, strengthens with time. In

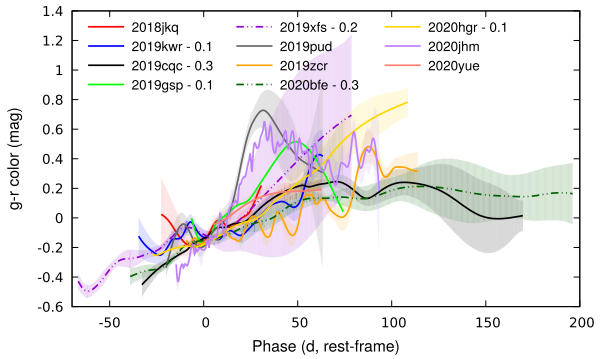

Figure 11. Our GP fits to the rest-frame $g - r$ colours of our sample objects when available. Constants have been added to roughly match peak-phase colours and emphasize the subsequent evolution. These constants may reflect intrinsic colour differences or low-to-moderate host galaxy extinction.

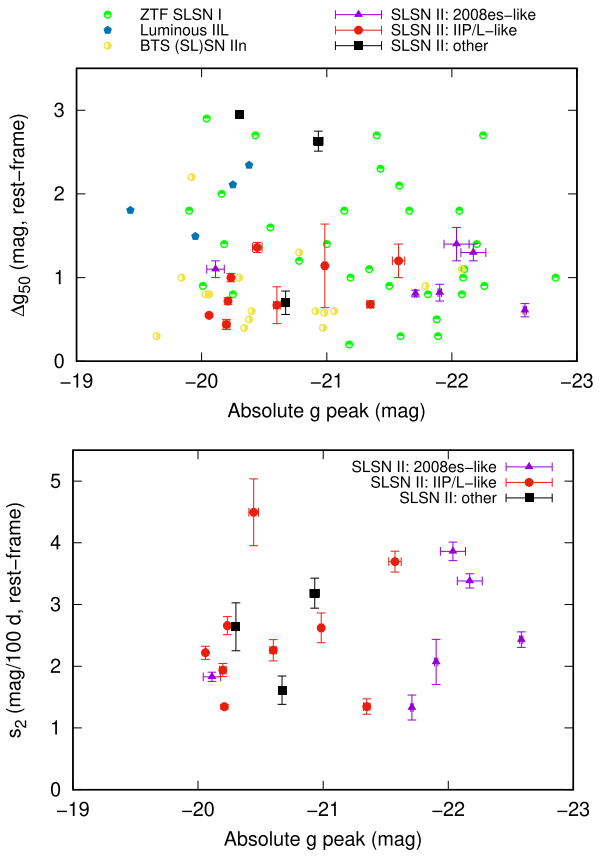

Figure 12. Top: decline rate characterized by the decline in 50 rest-frame days from the peak versus the absolute (rest-frame) g-band peak magnitudes of the SNe in our sample, CSS121015 (Benetti et al. 2014) and the SNe of Inserra et al. (2018). We also include groups of other publicly available SNe for comparison (de Vaucouleurs et al. 1981; Fassia et al. 2000; Kangas et al. 2016; Perley et al. 2020; Reynolds et al. 2020; Chen et al. 2022a). Bottom: decline rate s_2 (Anderson et al. 2014) versus g-band peak magnitude for the same SLSNe II.

SNe 2019pud and 2020yue, the SED is more consistent with a blackbody.

The shape of the UV SED is qualitatively similar to that of the luminous Type II-L SN 1979C (Panagia et al. 1980). Fransson et al. (1984) examined this spectrum and considered the UV excess to be a result of CSI; a forest of emission lines from various highly ionized species was caused by ionization and excitation by X-rays from the interaction (a similar UV spectrum was also seen for the Type IIn SN 2010jl and the Type Icn SN 2019hgp: Fransson et al. 2014; Dessart, Audit & Hillier 2015; Gal-Yam et al. 2022). The events used here show considerable variety in terms of spectra and light curves, including the slowest, fastest, faintest, and brightest events in the sample. This suggests that they may represent the bulk of our sample, although this cannot be ascertained.

4.5 Radiated energy

We have roughly estimated the total energies radiated in the UV and optical (as we lack infrared data) in our sample SNe through the following steps. Considering the UV excess, we cannot simply fit a blackbody to the observed SEDs. Instead, we have constructed the pseudo-bolometric light curves of SNe 2019zcr and 2020hgr, the objects in the sample with the best UV-to-optical coverage, both showing a clear UV excess. We have used our GP interpolated light curve at each filter to integrate over both wavelength and time using the trapezoidal approximation and setting the flux density to zero at the blue edge of the *UVW2* filter and at the *J* band. We fit a third-degree polynomial to the bolometric corrections we have obtained for both targets:

$$L_{\rm bol} = L_{gr,\rm RF}[A(g-r)^3_{\rm RF} + B(g-r)^2_{\rm RF} + C(g-r)_{\rm RF} + D]\,, \quad (2)$$

where $L_{\rm bol}$ is bolometric luminosity, $L_{gr,\rm RF}$ is the luminosity in the rest-frame g and r bands, and $(g-r)_{\rm RF}$ the rest-frame $g-r$ colour. We obtain $A = -42 \pm 11$, $B = 16 \pm 2$, $C = -2.8 \pm 0.4$, and $D = 1.95 \pm 0.03$.

We have then used these corrections to estimate the UV-to-optical pseudo-bolometric light curves of the less well-observed SNe in our sample and integrate these over time. This assumes that all SNe in the sample have similar UV excesses and thus only serves as an order-of-magnitude estimate. The resulting values can be considered rough lower limits for the total radiated energy as they ignore any infrared and far-UV contribution and are not extrapolated in time to unobserved epochs. We list the resulting radiated energies in Table 3.

5 LIGHT-CURVE MODELLING

5.1 Modelling setup

In order to fit various models to the light curves of our sample SLSNe, we used the publicly available code Modular Open Source Fitter for Transients (MOSFIT[9]; Guillochon et al. 2018). The code includes the ^{56}Ni decay model (Arnett 1982; Nadyozhin 1994), labelled `default`; a combination of CSI and ^{56}Ni decay (Chatzopoulos et al. 2013; Villar et al. 2017; Jiang, Jiang & Villar 2020), labelled `csmni`; and a combination of a magnetar and ^{56}Ni decay (Nicholl et al. 2017), labelled `magni`. These models are fitted using the dynamic nested sampling package DYNESTY.[10] We fitted each of these models for each SN. For the CSI models, we also fixed the parameter s (where the CSM density as a function of distance behaves as $\rho \propto r^{-s}$) to two values: $s = 0$ (indicating a CSM shell) and $s = 2$ (indicating a wind-like CSM).

We set simple uniform or log-uniform priors for each free parameter, listed in Table 4. We set the lower limit on the characteristic

[9] https://mosfit.readthedocs.io/en/latest/index.html
[10] https://dynesty.readthedocs.io/en/latest/

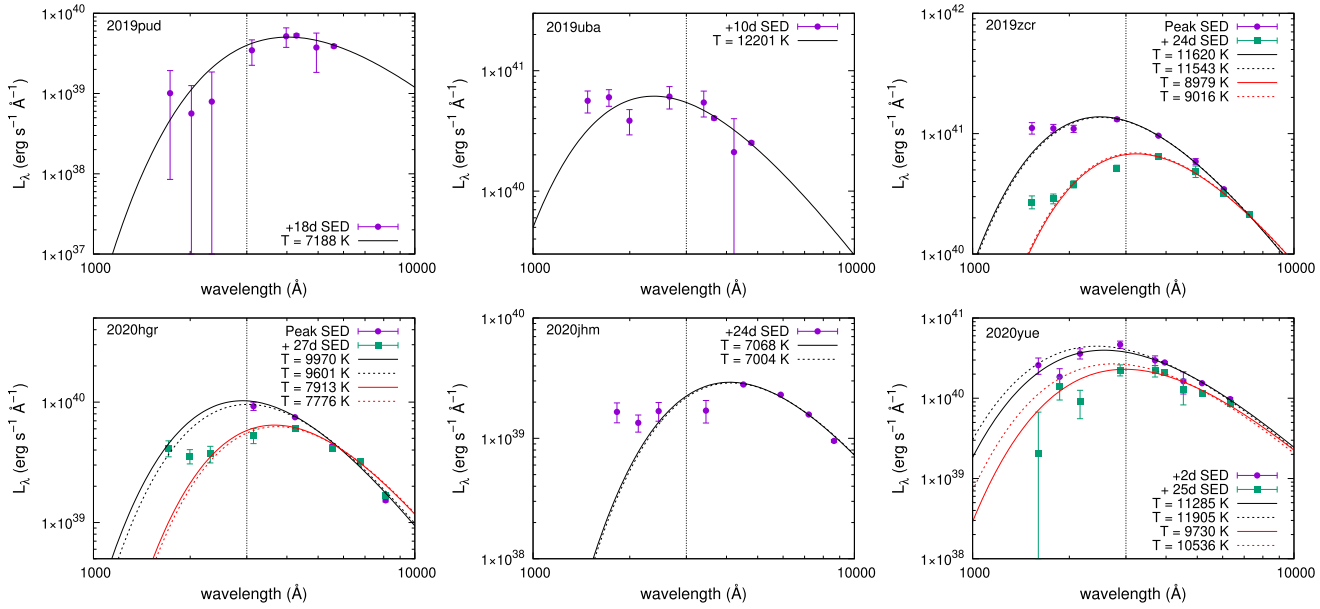

Figure 13. Blackbody fits (lines) using the combined UV and optical data when available (points). We use the peak epoch if possible; if not, we show the earliest possible epoch. For SNe 2019zcr, 2020hgr and 2020yue, we also perform the fit to UV data at ∼25 d. The dashed vertical line corresponds to the limit of the modified SED (Nicholl, Guillochon & Berger 2017) at 3000 Å. Dashed curves correspond to fits without the points below 3000 Å; these were performed for the SNe where the remaining points have the smallest errors. An excess at the UV wavelengths is immediately clear in four of the six events compared to the blackbody fit.

Table 3. Estimated total energies of the sample SNe radiated in the UV-to-optical range over the *observed* light curve. We assume all SNe here to have a UV excess similar to SNe 2019zcr and 2020hgr, which we use to estimate bolometric corrections.

SN	Radiated energy (erg)
SN 2019zcr	$>3.1 \times 10^{51}$
SN 2020hgr	$>3.7 \times 10^{50}$
SN 2018jkq	$\gtrsim 2.3 \times 10^{50}$
SN 2019kwr	$\gtrsim 2.4 \times 10^{50}$
SN 2019cqc	$\gtrsim 1.5 \times 10^{50}$
SN 2019gsp	$\gtrsim 2.3 \times 10^{50}$
SN 2019xfs	$\gtrsim 6.0 \times 10^{50}$
SN 2019pud	$\gtrsim 2.5 \times 10^{50}$
SN 2018lqi	$\gtrsim 2.2 \times 10^{50}$
SN 2019aanx	$\gtrsim 9.1 \times 10^{50}$
SN 2019uba	$\gtrsim 1.8 \times 10^{51}$
SN 2020bfe	$\gtrsim 2.6 \times 10^{50}$
SN 2020jhm	$\gtrsim 1.4 \times 10^{50}$
SN 2020yue	$\gtrsim 6.1 \times 10^{50}$

ejecta velocity to be the FWHM of the Hα emission (as this is often measured weeks after the peak), rounded down to the nearest 1000 km s^{-1}, and the upper limit at twice the lower limit, as listed in Table 5. Near-peak spectra with absorption lines from which to measure photospheric velocities are almost non-existent in our sample. We set the fraction of ^{56}Ni in the ejecta, $f_{\rm Ni}$, at a conservative value of $\leq$0.3. Based on the lack of narrow Na I D absorption lines in the spectra and on the colour variation within the sample described above, we also set an upper limit for the host galaxy extinction, $A_{V,\,\rm host} \leq 1$ mag. Host extinction itself is not a parameter in MOSFIT, but the column density of neutral hydrogen ($n_{H,\,\rm host}$) is, and can be used as a proxy. We therefore set the upper limit as $n_{H,\,\rm host} \leq 2 \times 10^{21}$ cm^{-2} based on Güver & Özel (2009).

Table 4. Priors of our MOSFIT runs. Each free parameter has either a uniform or log-uniform distribution as indicated.

Parameter	Range	Distribution
	Common parameters	
$n_{H,\,\rm host}$	$(10^{16} : 2 \times 10^{21})$ cm^{-2}	log-uniform
$f_{\rm Ni}$	$(10^{-3} : 0.3)$	log-uniform
$t_{\rm expl}$	$(-200 : 0)$ d	uniform
$T_{\rm min}$	$(1000 : 10^5)$ K	log-uniform
κ	0.34 cm^2 g^{-1}	fixed
κ_γ	$(0.1 : 10^4)$ cm^2 g^{-1}	log-uniform
	^{56}Ni model parameters	
$M_{\rm ej}$	$(0.1 : 100)$ M$_\odot$	log-uniform
	Magnetar + ^{56}Ni model parameters	
$P_{\rm spin}$	$(0.7 : 20)$ ms	uniform
$B_\perp$	$(0.05 : 50) \times 10^{14}$ G	log-uniform
$M_{\rm NS}$	$(1.0 : 2.5)$ M$_\odot$	uniform
$\theta_{\rm PB}$	$(0 : \pi/2)$ rad	uniform
$M_{\rm ej}$	$(3 : 100)$ M$_\odot$	log-uniform
	CSI + ^{56}Ni model parameters	
n	11	fixed
δ	1	fixed
s	0 or 2	fixed
R_0	$(0.1 : 1000)$ au	log-uniform
$M_{\rm CSM}$	$(0.1 : 100)$ M$_\odot$	log-uniform
$M_{\rm ej}$	$(0.1 : 100)$ M$_\odot$	log-uniform
ρ	$(10^{-15} : 10^{-6})$ cm^{-3}	log-uniform

The presence of hydrogen in the SN spectra is helpful for setting some of the priors. We fix the Thomson scattering opacity parameter

Table 5. Ejecta velocity priors of our MOSFIT runs. Each parameter has a uniform distribution between the indicated values.

SN	v_{ej} range (km s^{-1})
SN 2018jkq	(6000 : 12 000)
SN 2019kwr	(6000 : 12 000)
SN 2019cqc	(8000 : 16 000)
SN 2019gsp	(8000 : 16 000)
SN 2019xfs	(5000 : 10 000)
SN 2019pud	(10 000 : 20 000)
SN 2018lqi	(5000 : 10 000)
SN 2019aanx	(6000 : 12 000)
SN 2019uba	(8000 : 16 000)
SN 2019zcr	(7000 : 14 000)
SN 2020bfe	(8000 : 16 000)
SN 2020hgr	(7000 : 14 000)
SN 2020jhm	(12 000 : 24 000)
SN 2020yue	(11 000 : 22 000)

$\kappa = 0.34$ cm^2 g^{-1}, a typical value for hydrogen-rich ejecta and close to the results of Nagy (2018), in each model. In the CSI models, we assume a hydrogen-rich progenitor, but not necessarily an extended envelope such as that of a red supergiant (RSG). Thus the minimum inner radius of the CSM, R_0, is set at 0.1 au ($\sim 20 R_\odot$), roughly half the radius of the blue supergiant progenitor of SN 1987A (Podsiadlowski 1992) but larger than a Wolf–Rayet progenitor of a stripped-envelope SN. In the magnetar models, we can also set a minimum ejecta mass at roughly 3 M$_\odot$. For details on the magnetar model setup, see Appendix C.

Parameters common to all models include the explosion time before observations t_{expl}, the opacity to γ rays κ_γ and the minimum temperature T_{min}. For the magnetar model, the free parameters additionally include the spin period P_{spin}, the magnetic-field perpendicular to the spin axis $B_\perp$, the neutron star mass M_{NS}, and the angle between the magnetic field and spin axis θ_{PB}. In the CSI model, we additionally include the CSM mass M_{CSM} and the CSM density at R_0, ρ. We fix the density profile parameters in the inner and outer ejecta, $\delta = 1$ and $n = 11$, respectively. All parameters described above are summarized in Table 4 (all parameters except v_{ej}) and Table 5 (individual v_{ej} for each SN). In total, the `default` model has 8 free parameters, the `magni` model has 12 and, the `csmni` model has 11. These numbers include a nuisance parameter σ, which describes the added variance required to match the model being fitted. We ran each fitting process until convergence.

5.2 Modelling results

We include the light curves and corner plots for our MOSFIT modelling as supplementary material, available online. The median posterior parameter values and their 1σ errors for each SN and model are presented in Tables 6, 7, 8 and 9. MOSFIT determines a likelihood score (based on the Watanabe–Akaike Information Criterion; Watanabe 2010) for each posterior ensemble. Higher values indicate a better fit, and scores are comparable between models with different numbers of free parameters (see Guillochon et al. 2018).

^{56}Ni decay alone cannot reproduce our light curves. The nickel fraction f_{Ni} gravitates towards its maximum allowed value. Combined with the large required ejecta masses (typically tens of M$_\odot$), this results in extremely high ^{56}Ni masses, while the observed light-curve evolution is faster than such large ejecta masses would require. The likelihood scores determined by MOSFIT are the lowest for the ^{56}Ni model, with the exception of SN 2020hgr, for which we do not obtain a good fit with any model in the UV (see below). Therefore, we rule out ^{56}Ni decay as the dominant power source.

A few objects with UV data are problematic for all of the models; these are SNe 2020hgr, 2020jhm, and 2020yue. SNe 2020hgr and 2020yue show a fast-declining UV light curve that is not reproduced by either the magnetar or CSM models, while UV points of SN 2020jhm are underpredicted in both models. This does not apply to all UV data, however, SNe 2019xfs, 2019pud, 2019uba, and 2019zcr also include UV data and are reproduced by both magnetar and CSM models. This is despite the observed UV excess in SN 2019zcr. The UV discrepancy does not necessarily pose a problem: both models could have trouble reproducing the UV light curve if, e.g. the 1D Chatzopoulos et al. (2013) model cannot account for all the mechanisms at play in the interaction. It has been shown that this model can produce light curves an order of magnitude different than those from more detailed, numerical CSI models (Sorokina et al. 2016). Overall, most of the sample remains consistent with both magnetar and CSI power sources. The likelihood scores are lowest for ^{56}Ni decay, but the difference between the CSI and magnetar scores is $\lesssim$20 per cent, usually $<$10 per cent. Therefore we cannot distinguish between these power sources based on the score, nor between different CSI models where $s = 0$ or $s = 2$. A similar ambiguity in the power source based on light curves alone was found by Chen et al. (2022b) for a large sample of SLSNe I.

6 HOST GALAXY PROPERTIES

The properties of the host galaxies of the SNe in our sample can shed light on their progenitors. The hosts of previously studied SLSNe II were faint, presumably metal-poor dwarf galaxies (Inserra et al. 2018; Schulze et al. 2018) similar to those of SLSNe I, whereas SLSNe IIn occupy a wider range in metallicity, stellar mass, and brightness (Perley et al. 2016; Schulze et al. 2021). Here we perform a comparison between previous studies of SN host galaxies and our sample by fitting stellar population models to host galaxy photometry.

We have retrieved science-ready co-added images of the host galaxies from the *Galaxy Evolution Explorer* (*GALEX*) general release 6/7 (Martin et al. 2005), the Sloan Digital Sky Survey data release 9 (SDSS DR 9; Ahn et al. 2012), DESI Legacy Imaging Surveys (Legacy Surveys; Dey et al. 2019) data release 8, the data archive of the 3.6 m Canada–France–Hawaii Telescope[11] (USA), and *WISE* images (Wright et al. 2010) from the unWISE archive (Lang 2014).[12] The unWISE images are based on the public *WISE* data and include images from the ongoing NEOWISE-Reactivation mission R3 (Mainzer et al. 2014; Meisner, Lang & Schlegel 2017). For SNe 2019cqc, 2020jhm, and 2020yue, we augmented the SEDs with UV and optical data obtained with the *Swift*/UVOT in 2021 October, after the SNe had faded.

The brightness of each host galaxy was measured using Lambda Adaptive Multi-Band Deblending Algorithm in R (`LAMBDAR`)[13] (Wright et al. 2016) and the methods described in Schulze et al. (2021). The photometry on the UVOT images was done with `uvotsource` in HEASOFT and using an aperture encircling the entire galaxy. All magnitudes were transformed into the AB system using Breeveld et al. (2011b) and Cutri et al. (2013, their table 3).

[11] https://www.cadc-ccda.hia-iha.nrc-cnrc.gc.ca/en/cfht/
[12] http://unwise.me
[13] https://github.com/AngusWright/LAMBDAR

Table 6. Most important MOSFIT parameters and scores for the ^{56}Ni powered model.

SN	$\log f_{\rm Ni}$	$\log M_{\rm ej}$ ($M_\odot$)	$\log T_{\rm min}$ (K)	$v_{\rm ej}$ (km s^{-1})	Score
SN 2018jkq	$-0.56^{+0.03}_{-0.04}$	1.8 ± 0.1	4.00 ± 0.04	$11\,000^{+700}_{-1300}$	-8.5
SN 2019kwr	-0.53 ± 0.01	1.38 ± 0.02	3.96 ± 0.01	$11\,900^{+100}_{-200}$	270.7
SN 2019cqc	-0.53 ± 0.01	1.34 ± 0.01	3.87 ± 0.01	$15\,900^{+100}_{-200}$	398.6
SN 2019gsp	$-0.57^{+0.03}_{-0.06}$	1.8 ± 0.2	3.97 ± 0.04	$14\,400^{+1200}_{-2000}$	-3.3
SN 2019xfs	$-0.55^{+0.02}_{-0.04}$	1.5 ± 0.1	3.89 ± 0.02	9400^{+500}_{-900}	-37.3
SN 2019pud	-0.6 ± 0.1	1.8 ± 0.2	3.84 ± 0.03	$16\,700^{+2100}_{-3100}$	-15.5
SN 2018lqi	$-0.56^{+0.02}_{-0.04}$	1.84 ± 0.09	3.98 ± 0.04	9200^{+600}_{-900}	-0.1
SN 2019aanx	-0.53 ± 0.01	1.99 ± 0.01	3.96 ± 0.02	$11\,800^{+200}_{-300}$	57.9
SN 2019uba	-0.53 ± 0.01	1.99 ± 0.01	4.04 ± 0.02	$15\,700^{+200}_{-500}$	-33.7
SN 2019zcr	-0.53 ± 0.01	1.99 ± 0.01	4.02 ± 0.02	$13\,800^{+200}_{-300}$	-180.3
SN 2020bfe	-0.53 ± 0.01	1.35 ± 0.02	3.86 ± 0.01	$15\,600^{+300}_{-500}$	147.7
SN 2020hgr	-0.53 ± 0.01	1.38 ± 0.01	3.98 ± 0.01	$13\,900^{+100}_{-200}$	332.9
SN 2020jhm	-0.52 ± 0.01	0.64 ± 0.01	3.89 ± 0.01	$23\,900 \pm 100$	-34.6
SN 2020yue	-0.52 ± 0.01	1.99 ± 0.01	4.02 ± 0.01	$23\,900^{+100}_{-200}$	187.7

Table 7. Most important MOSFIT parameters and scores for the magnetar-powered model with ^{56}Ni.

SN	$\log B_\perp$ (10^{14} G)	$M_{\rm NS}$ ($M_\odot$)	$P_{\rm spin}$ (ms)	$\log f_{\rm Ni}$	$\log M_{\rm ej}$ ($M_\odot$)	θ_{PB} (rad)	$v_{\rm ej}$ (km s^{-1})	Score
SN 2018jkq	$0.5^{+0.2}_{-0.3}$	1.7 ± 0.4	$1.9^{+0.9}_{-0.7}$	$-2.1^{+0.7}_{-0.6}$	0.9 ± 0.1	$0.8^{+0.4}_{-0.3}$	7700 ± 500	53.7
SN 2019kwr	0.4 ± 0.2	$1.3^{+0.3}_{-0.2}$	$1.5^{+0.9}_{-0.5}$	-2.4 ± 0.4	$0.96^{+0.04}_{-0.06}$	$0.9^{+0.4}_{-0.3}$	7500^{+200}_{-300}	741.5
SN 2019cqc	0.9 ± 0.2	$2.1^{+0.3}_{-0.4}$	$2.0^{+0.8}_{-0.7}$	$-0.54^{+0.01}_{-0.02}$	0.93 ± 0.01	0.7 ± 0.2	8100 ± 100	724.7
SN 2019gsp	0.7 ± 0.2	1.9 ± 0.4	$2.0^{+1.1}_{-0.9}$	$-2.1^{+0.5}_{-0.6}$	0.65 ± 0.05	1.0 ± 0.3	8500^{+600}_{-400}	66.8
SN 2019xfs	0.2 ± 0.2	$1.9^{+0.4}_{-0.4}$	$1.0^{+0.3}_{-0.2}$	$-1.6^{+0.4}_{-0.5}$	0.96 ± 0.04	0.9 ± 0.3	5800^{+200}_{-300}	58.4
SN 2019pud	0.8 ± 0.3	1.7 ± 0.5	3 ± 2	$-0.6^{+0.1}_{-0.2}$	$0.53^{+0.05}_{-0.04}$	0.9 ± 0.4	$16\,700^{+1900}_{-1500}$	13.1
SN 2018lqi	0.2 ± 0.3	1.8 ± 0.5	$5.0^{+1.0}_{-1.1}$	$-1.4^{+0.6}_{-1.0}$	0.6 ± 0.1	0.9 ± 0.4	6200 ± 400	72.2
SN 2019aanx	-0.2 ± 0.3	$2.0^{+0.4}_{-0.5}$	$2.6^{+0.5}_{-0.6}$	$-1.8^{+0.9}_{-0.8}$	$1.0^{+0.3}_{-0.2}$	$0.9^{+0.5}_{-0.5}$	$10\,200 \pm 700$	117.8
SN 2019uba	$-0.1^{+0.2}_{-0.3}$	1.7 ± 0.4	2.5 ± 0.6	$-2.2^{+0.8}_{-0.5}$	$0.51^{+0.04}_{-0.02}$	0.9 ± 0.3	9300^{+1200}_{-700}	65.7
SN 2019zcr	-0.2 ± 0.2	$1.8^{+0.5}_{-0.6}$	$2.0^{+0.4}_{-0.5}$	$-2.1^{+0.8}_{-0.6}$	0.69 ± 0.03	0.6 ± 0.4	$11\,300 \pm 300$	232.7
SN 2020bfe	$-0.0^{+0.2}_{-0.3}$	1.8 ± 0.5	$5.7^{+1.0}_{-1.1}$	$-1.4^{+0.6}_{-1.1}$	0.89 ± 0.03	$1.1^{+0.3}_{-0.4}$	8100^{+200}_{-100}	215.6
SN 2020hgr	-0.1 ± 0.2	$2.2^{+0.3}_{-0.4}$	$4.2^{+1.4}_{-0.9}$	$-0.7^{+0.1}_{-0.2}$	1.3 ± 0.1	0.9 ± 0.4	$12\,200^{+1400}_{-2400}$	354.6
SN 2020jhm	$1.1^{+0.1}_{-0.2}$	$2.1^{+0.3}_{-0.5}$	$0.8^{+0.3}_{-0.1}$	-1.02 ± 0.05	0.54 ± 0.02	$1.2^{+0.2}_{-0.3}$	$16\,900^{+600}_{-800}$	780.3
SN 2020yue	-0.3 ± 0.2	$1.7^{+0.4}_{-0.5}$	$3.5^{+0.6}_{-0.7}$	$-1.6^{+0.7}_{-0.8}$	$0.8^{+0.1}_{-0.2}$	1.0 ± 0.3	$18\,000^{+3700}_{-4600}$	332.2

In the case of SN 2019xfs, which is located $\sim$1.″8 from an 18th magnitude star, we removed the star with `galfit` (Peng et al. 2010). We measured the flux at the explosion site using the aperture photometry tool presented in Schulze et al. (2018).

For the fitting itself, we used the PROSPECTOR package,[14] version 0.3 (Leja et al. 2017), to model the SEDs of the host galaxies and extract their physical parameters. PROSPECTOR uses the Flexible Stellar Population Synthesis (`FSPS`[15]) code (Conroy, Gunn & White 2009) for the physical model and `python-fsps`[16] (Foreman-Mackey, Sick & Johnson 2014) for a PYTHON-based interface. For details about the model setup, see Schulze et al. (2021); we performed these fits in an identical manner with the same assumptions and priors.

The results of the fitting process are listed for each host galaxy in Table 10. We compare the stellar masses and star-formation rates (SFRs) of our sample to those of SLSNe I, SLSNe IIn, and normal SNe II from Schulze et al. (2021) in Fig. 14, also including the host galaxies of SNe 2008es and 2013hx from Schulze et al. (2018). To address cosmic evolution and make the normal SN II sample more comparable to ours, we only include the SNe II with $z > 0.08$, corresponding roughly to the most distant 10 per cent. The SLSN II hosts in general overlap strongly with those of both SLSNe IIn and SLSNe I. While there is overlap with normal SNe II as well, the SLSN II hosts preferentially seem to be somewhat less massive and more strongly star forming than them or the galaxy main sequence (Lee et al. 2015).

We have investigated possible differences using two-sample Anderson–Darling tests with the distributions of absolute magnitude, stellar mass, SFR, and specific SFR (sSFR); here, we have also included the host galaxies of normal SNe Ibc and IIn from Schulze et al. (2021), applying the same distance cut of $z > 0.08$. The test results are listed in Table 11. The host galaxies of SLSNe II are consistent with those of SLSNe IIn in terms of all four properties, and the p-values are all >0.6, suggesting a strong overlap. The sSFRs of the SLSN II hosts are individually inconsistent at the 95 per cent confidence level with being drawn from the same distributions as the sSFRs of SLSN I and SN II hosts. However, the results are affected by the presence of multiple 'null' hypotheses, all of which must

[14] https://github.com/bd-j/prospector
[15] https://github.com/cconroy20/fsps
[16] https://dfm.io/python-fsps/current/

Table 8. Most important MOSFIT parameters and scores for the CSM + Ni model when $s = 2$. The kinetic energy E_k is calculated separately as $E_k = 0.3 M_{\rm ej} v_{\rm ej}^2$ and is not a model parameter.

SN	$\log f_{\rm Ni}$	$\log M_{\rm CSM}$ ($M_\odot$)	$\log M_{\rm ej}$ ($M_\odot$)	$\log R_0$ (au)	$\log \rho$ (g cm^{-3})	$v_{\rm ej}$ (km s^{-1})	E_k (10^{51} erg)	Score
SN 2018jkq	$-0.8^{+0.2}_{-0.3}$	$0.6^{+0.3}_{-0.2}$	0.6 ± 0.5	1.1 ± 0.6	$-10.7^{+1.0}_{-0.9}$	8000 ± 500	$1.7^{+3.0}_{-1.1}$	62.1
SN 2019kwr	-1.7 ± 0.2	$-0.38^{+0.06}_{-0.05}$	1.62 ± 0.04	$0.84^{+0.06}_{-0.07}$	-10.1 ± 0.2	7700 ± 200	15 ± 2	739.2
SN 2019cqc	$-1.3^{+0.7}_{-1.4}$	$-0.1^{+0.3}_{-0.1}$	$0.3^{+0.3}_{-0.5}$	$1.4^{+0.3}_{-0.1}$	$-9.1^{+0.1}_{-0.2}$	8200 ± 200	0.8 ± 0.5	696.4
SN 2019gsp	$-1.8^{+0.9}_{-0.7}$	$-0.2^{+0.3}_{-0.4}$	$0.4^{+0.6}_{-0.7}$	$1.6^{+0.3}_{-0.4}$	$-9.3^{+1.1}_{-0.40}$	8600^{+500}_{-400}	$1.0^{+3.1}_{-0.9}$	72.2
SN 2019xfs	$-1.6^{+0.7}_{-0.9}$	0.5 ± 0.4	$0.1^{+0.6}_{-0.7}$	2.0 ± 0.4	$-8.4^{+0.5}_{-0.4}$	5300^{+300}_{-200}	$3.2^{+1.1}_{-0.8}$	52.4
SN 2019pud	$-1.1^{+0.2}_{-0.1}$	$-0.7^{+0.3}_{-0.2}$	1.4 ± 0.2	$1.3^{+0.3}_{-0.2}$	$-10.1^{+1.2}_{-1.1}$	$12\,700 \pm 900$	23^{+10}_{-8}	15.2
SN 2018lqi	-1.8 ± 0.8	-0.3 ± 0.4	-0.0 ± 0.7	1.3 ± 0.4	$-8.1^{+0.9}_{-0.5}$	6400^{+500}_{-400}	$0.2^{+0.9}_{-0.2}$	68.4
SN 2019aanx	$-2.0^{+1.0}_{-0.7}$	$1.29^{+0.10}_{-0.04}$	$-0.1^{+0.4}_{-0.2}$	$-0.2^{+2.2}_{-0.6}$	-8^{+2}_{-5}	$11\,200^{+600}_{-800}$	$0.6^{+0.5}_{-0.2}$	120.0
SN 2019uba	$-0.56^{+0.02}_{-0.04}$	$0.42^{+0.06}_{-0.07}$	$1.9^{+0.1}_{-0.2}$	$0.2^{+0.8}_{-0.7}$	-9 ± 2	$11\,100 \pm 400$	53 ± 4	88.3
SN 2019zcr	$-1.8^{+0.6}_{-0.8}$	1.4 ± 0.2	0.1 ± 0.5	$2.6^{+0.3}_{-0.4}$	$-13.3^{+0.5}_{-0.3}$	$11\,900 \pm 200$	$1.0^{+1.7}_{-0.7}$	228.1
SN 2020bfe	$-1.1^{+0.2}_{-0.4}$	$0.6^{+0.1}_{-0.2}$	$0.4^{+0.3}_{-0.2}$	$1.7^{+0.1}_{-0.2}$	$-11.0^{+0.4}_{-0.3}$	8400 ± 200	$1.1^{+0.8}_{-0.3}$	181.4
SN 2020hgr	$-0.7^{+0.2}_{-0.9}$	$-0.4^{+0.5}_{-0.4}$	$1.1^{+0.2}_{-0.9}$	$0.8^{+0.5}_{-0.4}$	-7.7 ± 0.4	7700^{+800}_{-500}	$3.9^{+1.9}_{-3.4}$	310.1
SN 2020jhm	$-0.9^{+0.2}_{-0.9}$	$-0.3^{+0.1}_{-0.5}$	$0.2^{+0.9}_{-0.2}$	$1.7^{+0.1}_{-0.5}$	$-11.0^{+0.9}_{-0.4}$	$12\,500^{+300}_{-200}$	$1.6^{+8.5}_{-0.5}$	854.9
SN 2020yue	$-1.9^{+0.7}_{-0.6}$	$-0.3^{+0.6}_{-0.3}$	$0.9^{+0.5}_{-0.9}$	$1.1^{+0.5}_{-0.3}$	$-9.4^{+0.3}_{-0.7}$	$13\,400^{+1200}_{-1100}$	9^{+14}_{-8}	345.4

Table 9. Most important MOSFIT parameters and scores for the CSM + Ni model when $s = 0$. The kinetic energy E_k is calculated separately as $E_k = 0.3 M_{\rm ej} v_{\rm ej}^2$ and is not a model parameter.

SN	$\log f_{\rm Ni}$	$\log M_{\rm CSM}$ ($M_\odot$)	$\log M_{\rm ej}$ ($M_\odot$)	$\log R_0$ (au)	$\log \rho$ (g cm^{-3})	$v_{\rm ej}$ (km s^{-1})	E_k (10^{51} erg)	Score
SN 2018jkq	-1.2 ± 0.4	0.7 ± 0.2	$0.8^{+0.3}_{-0.2}$	1.0 ± 0.8	$-11.7^{+0.6}_{-0.4}$	8800^{+600}_{-1100}	$2.7^{+1.6}_{-1.1}$	53.3
SN 2019kwr	$-2.2^{+0.3}_{-0.6}$	0.9 ± 0.2	$1.16^{+0.06}_{-0.05}$	2.4 ± 0.2	$-10.96^{+0.06}_{-0.07}$	6800 ± 200	$4.0^{+0.6}_{-0.5}$	730.9
SN 2019cqc	$-1.6^{+0.7}_{-0.9}$	$1.2^{+0.2}_{-0.3}$	$-0.3^{+0.6}_{-0.5}$	$2.5^{+0.2}_{-0.3}$	$-6.7^{+0.4}_{-0.5}$	8000 ± 100	$0.2^{+0.5}_{-0.2}$	694.7
SN 2019gsp	-2.8 ± 0.2	$-0.2^{+0.2}_{-0.4}$	0.9 ± 0.2	$0.4^{+0.4}_{-0.6}$	$-11.5^{+0.8}_{-0.4}$	9900 ± 400	4.3 ± 1.0	67.7
SN 2019xfs	-2.5 ± 0.4	$0.81^{+0.06}_{-0.04}$	1.60 ± 0.06	$1.3^{+0.9}_{-1.4}$	$-12.7^{+0.2}_{-0.1}$	5900^{+200}_{-300}	9^{+2}_{-1}	52.6
SN 2019pud	-0.70 ± 0.07	-0.34 ± 0.08	1.0 ± 0.2	$0.4^{+0.7}_{-0.8}$	-12.5 ± 0.2	$11\,000^{+700}_{-600}$	8 ± 3	18.4
SN 2018lqi	$-1.4^{+0.5}_{-0.6}$	$0.76^{+0.04}_{-0.06}$	$1.19^{+0.05}_{-0.06}$	$0.3^{+1.1}_{-0.9}$	$-12.61^{+0.06}_{-0.09}$	5500 ± 200	2.8 ± 0.3	79.7
SN 2019aanx	-1.9 ± 0.8	1.37 ± 0.04	0.8 ± 0.2	$1.0^{+1.0}_{-1.1}$	-12.9 ± 0.1	9500 ± 700	$3.4^{+1.1}_{-0.9}$	122.2
SN 2019uba	$-0.55^{+0.02}_{-0.03}$	-0.1 ± 0.1	1.64 ± 0.07	$0.4^{+0.6}_{-0.7}$	-11.7 ± 0.2	9400^{+800}_{-700}	23 ± 2	85.2
SN 2019zcr	-1.1 ± 0.4	$1.2^{+0.2}_{-0.1}$	$1.4^{+0.1}_{-0.2}$	2.5 ± 0.2	$-13.1^{+0.3}_{-0.1}$	$10\,200 \pm 300$	13^{+2}_{-5}	236.9
SN 2020bfe	-1.8 ± 0.8	1.3 ± 0.3	-0.1 ± 0.6	$2.4^{+0.2}_{-0.3}$	$-7.4^{+0.5}_{-0.6}$	8100^{+200}_{-100}	$0.3^{+0.9}_{-0.3}$	200.4
SN 2020hgr	-1.7 ± 0.8	1.49 ± 0.04	$1.1^{+0.2}_{-0.4}$	0.9 ± 1.2	-13.0 ± 0.1	8100^{+900}_{-600}	5^{+2}_{-3}	380.3
SN 2020jhm	$-1.38^{+0.03}_{-0.02}$	$-0.93^{+0.02}_{-0.03}$	0.66 ± 0.02	$-0.3^{+0.6}_{-0.5}$	$-10.82^{+0.06}_{-0.03}$	$12\,100^{+200}_{-100}$	4.0 ± 0.2	853.6
SN 2020yue	$-1.6^{+0.7}_{-0.8}$	1.0 ± 0.3	$0.2^{+0.6}_{-0.8}$	2.2 ± 0.3	$-9.2^{+0.7}_{-0.6}$	$12\,200^{+200}_{-100}$	$1.4^{+3.3}_{-1.2}$	325.8

be true simultaneously for two galaxy distributions to be the same. We apply the Bonferroni correction and adjust the confidence level accordingly, with $m = 4$ as we test four properties in each host galaxy comparison. This means that, for a 95 per cent confidence level, a significant difference in galaxy properties now requires $p < 0.05/4$. Thus no significant differences are seen between any other hosts and those of SLSNe II; likely as a result of our relatively small sample. We also note that this is despite the filter algorithm favouring blue, faint hosts for SLSN candidates (Section 2).

Our full sample includes several events that spectroscopically resemble normal SNe II more than they resemble SN 2008es. It is possible that the 08es-like subgroup (i.e. those with a symmetric, broad Hα line and weak absorption features) has host galaxies similar to SLSNe I, as suggested by Inserra et al. (2018). There are, unfortunately, not enough such SNe for a meaningful Anderson–Darling test. By eye, the 08es-like SNe from ZTF occupy the high-mass portion of the SLSN I host distribution in Fig. 14 and seem to prefer higher SFRs than the SNe II or SLSNe IIn – however, SN 2008es itself occurred in an extremely low-mass, low-SFR host.

7 DISCUSSION

7.1 SLSNe II as a SN type

As stated above, we refer to our sample SNe as SLSNe II, as opposed to events of similar luminosity with narrow Balmer lines, which we refer to as SLSNe IIn. This follows Inserra et al. (2018) and is broadly consistent with the definition by Gal-Yam (2019), who described the features of SLSNe II in a similar way based on the four events known at the time. SLSNe I can be distinguished

Table 10. Results from the host galaxy SED modelling with PROSPECTOR. The absolute magnitudes are not corrected for host reddening. The SFRs are corrected for host reddening. For the host attenuation $E_{\rm host}(B-V)$, we used the Calzetti et al. (2000) model. The age refers to the age of the stellar population.

SN	Redshift	χ^2/d.o.f.	$E_{\rm host}(B-V)$ (mag)	M_B (mag)	log SFR ($M_\odot$ yr^{-1})	log M ($M_\odot$)	log sSFR (yr^{-1})	Age (Gyr)
SN 2018jkq	0.119	25.56/20	$0.10^{+0.08}_{-0.05}$	$-20.73^{+0.08}_{-0.04}$	$0.0^{+0.3}_{-0.2}$	$10.2^{+0.2}_{-0.1}$	$-10.2^{+0.4}_{-0.2}$	$2.4^{+2.4}_{-1.0}$
SN 2019kwr	0.202	9.77/9	$0.3^{+0.2}_{-0.1}$	$-18.8^{+0.2}_{-0.1}$	$0.2^{+0.5}_{-0.3}$	$9.5^{+0.2}_{-0.4}$	$-9.3^{+0.9}_{-0.4}$	$4.4^{+5.4}_{-3.8}$
SN 2019cqc	0.117	28.05/15	$0.12^{+0.06}_{-0.05}$	$-19.85^{+0.08}_{-0.04}$	0.1 ± 0.2	$9.8^{+0.2}_{-0.3}$	$-9.7^{+0.6}_{-0.2}$	7^{+5}_{-6}
SN 2019gsp	0.171	0.73/3	$0.3^{+0.3}_{-0.2}$	$-16.2^{+0.3}_{-0.2}$	$-0.5^{+0.8}_{-0.6}$	$7.9^{+0.5}_{-0.7}$	$-8.4^{+1.2}_{-0.9}$	$0.5^{+2.8}_{-0.5}$
SN 2019xfs	0.116	0.70/2	$0.6^{+0.4}_{-0.3}$	$-16.5^{+0.7}_{-0.4}$	$0.3^{+1.0}_{-0.9}$	$7.9^{+0.7}_{-0.6}$	$-7.5^{+1.2}_{-1.4}$	$0.1^{+1.4}_{-0.1}$
SN 2019pud	0.114	3.85/2	$0.9^{+0.8}_{-0.7}$	-12^{+5}_{-2}	$-1.1^{+1.3}_{-1.5}$	$6.9^{+1.4}_{-1.3}$	-8 ± 2	$0.3^{+4.0}_{-0.3}$
SN 2018lqi	0.202	9.55/7	$0.2^{+0.2}_{-0.1}$	$-18.57^{+0.09}_{-0.05}$	$-0.1^{+0.5}_{-0.3}$	$9.1^{+0.2}_{-0.3}$	$-9.2^{+0.8}_{-0.4}$	4^{+5}_{-3}
SN 2019aanx	0.403	1.44/3	$0.2^{+0.4}_{-0.2}$	$-18.8^{+0.4}_{-0.3}$	$0.6^{+0.8}_{-0.5}$	$8.3^{+0.8}_{-0.7}$	$-7.6^{+1.1}_{-1.0}$	$0.1^{+0.8}_{-0.1}$
SN 2019uba	0.303	2.51/3	$0.6^{+0.3}_{-0.2}$	$-17.3^{+0.5}_{-0.3}$	$0.7^{+0.5}_{-0.7}$	$8.6^{+0.8}_{-0.9}$	$-7.8^{+1.1}_{-1.2}$	$0.1^{+1.6}_{-0.1}$
SN 2019zcr	0.26	9.94/3	$0.8^{+0.6}_{-0.50}$	$-15.5^{+0.8}_{-0.5}$	$0.3^{+1.3}_{-1.2}$	$8.6^{+0.9}_{-1.2}$	$-8.2^{+1.4}_{-1.3}$	$0.4^{+3.5}_{-0.4}$
SN 2020bfe	0.099	9.42/12	$0.17^{+0.08}_{-0.04}$	$-20.3^{+0.3}_{-0.1}$	0.4 ± 0.2	$10.1^{+0.2}_{-0.4}$	$-9.7^{+0.7}_{-0.2}$	7 ± 5
SN 2020hgr	0.126	2.98/8	$0.1^{+0.2}_{-0.1}$	$-17.1^{+0.2}_{-0.1}$	$-0.6^{+0.4}_{-0.3}$	$8.0^{+0.4}_{-0.5}$	$-8.5^{+0.7}_{-0.6}$	$0.7^{+1.8}_{-0.6}$
SN 2020jhm	0.057	23.74/16	$0.13^{+0.08}_{-0.04}$	$-19.2^{+0.4}_{-0.1}$	$-0.3^{+0.4}_{-0.2}$	$9.6^{+0.2}_{-0.5}$	$-9.9^{+1.0}_{-0.3}$	4^{+5}_{-4}
SN 2020yue	0.204	15.86/20	$0.07^{+0.14}_{-0.06}$	-20.29 ± 0.03	$0.2^{+0.4}_{-0.2}$	$10.4^{+0.1}_{-0.3}$	$-10.1^{+0.6}_{-0.3}$	11^{+3}_{-6}

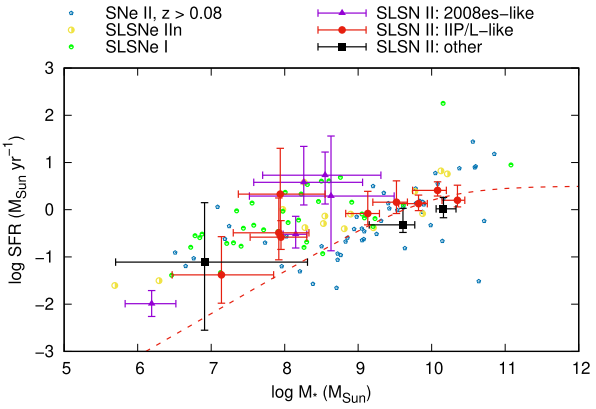

Figure 14. Host galaxies of SLSNe II compared to those of SLSNe I and IIn and normal SNe II from Schulze et al. (2021) in terms of stellar mass and SFR. We also include the hosts of SNe 2008es and 2013hx (Schulze et al. 2018). The red-dashed line corresponds to the galaxy main sequence (with parameters extrapolated to $z = 0.2$; Lee et al. 2015).

Table 11. Results (p-values) of our Anderson–Darling tests between the listed host galaxy properties of our sample SNe and earlier published SLSNe II from Schulze et al. (2018; total N = 17), and comparison subsamples of Schulze et al. (2021).

		SLSN II host properties			
Host sample	N	M_B	log M	log SFR	log sSFR
SLSNe IIn	14	0.85	0.86	0.63	0.70
SLSNe I	36	0.36	0.17	0.68	0.03
SNe II ($z > 0.08$)	51	0.17	0.13	0.46	0.02
SNe IIn ($z > 0.08$)	48	0.25	0.14	0.97	0.05
SNe Ibc ($z > 0.08$)	31	0.20	0.52	0.84	0.17

from other events based on spectra alone (Quimby et al. 2018), and on occasion overlap with other H-poor SNe in luminosity (Gomez et al. 2022). Our sample of SLSNe II has, instead, been constructed simply by including all SNe in ZTF phase I with peak magnitudes ≤ -20 mag, broad Hα emission and a lack of strong narrow lines, therefore constituting a less robust and more heterogeneous group (see Section 3). The sample includes SNe with peaks ranging from -20 mag to the extremely bright SN 2019zcr at ~ -22.6 mag. Few transients have reached a greater brightness, and these include SN 2015lh (Dong et al. 2016), likely a tidal disruption event (Leloudas et al. 2016), and three nuclear transients whose SN nature has not been ascertained (Kankare et al. 2017).

We have, however, shown that with the exception of SN 2020jhm, objects in our sample spectroscopically resemble less luminous SNe II. The relatively weak absorption lines, especially a lack of strong P Cygni absorption in Hα, and the late emergence of the strong Hα line in most cases, point towards SNe II-L similar to SNe 1979C and 1998S (e.g. Panagia et al. 1980; Fassia et al. 2001), although SN 2020yue is more similar to a Type II-P. The late-time spectra, however, lack strong forbidden lines of [O I] and [Ca II] usually seen in SNe II (e.g. Dessart & Hillier 2020). A plateau or bump phase typical to normal SNe II is not observed, and apart from two spectroscopically peculiar SLSNe II, SNe II-L decline faster at early times. Instead, the light curves of SLSNe II resemble those of other SLSNe. This is in agreement with previous work on SLSNe II (Inserra et al. 2018). Meanwhile, luminous SNe II-L, such as SN 2013fc (Kangas et al. 2016), would be included in this sample if they were present. Their absence indicates that they are rare among ZTF targets.

Observationally, we also note that only a minority of the sample resembles the prototypical SLSN II, SN 2008es (Gezari et al. 2009; Miller et al. 2009), more than normal SNe II; specifically, these 08es-like SNe exhibit more symmetric Hα profiles (at all epochs studied here), typically brighter peaks and weaker absorption lines than the rest of the sample. Despite constituting three of the four previously studied SLSNe II – as SN 2013hx (Inserra et al. 2018) can be considered a member of the other subgroup – these SNe thus seem less common than the SLSNe II more reminiscent of normal SNe II. We point out, however, that these subgroups may be connected by a continuum of properties. Since we define the sample based on a somewhat arbitrary luminosity limit, some degree of overlap or continuum with other H-rich SN subtypes may be expected as well.

Table 12. Most important MOSFIT parameters and scores for models re-run with $f_{\rm Ni} < 0.05$.

Magnetar fit	$\log B_\perp$ (10^{14} G)	$M_{\rm NS}$ ($M_\odot$)	$P_{\rm spin}$ (ms)	$\log f_{\rm Ni}$	$\log M_{\rm ej}$ ($M_\odot$)	θ_{PB} (rad)	$v_{\rm ej}$ (km s^{-1})	Score
SN 2019cqc	$0.4^{+0.3}_{-0.4}$	$1.9^{+0.5}_{-0.6}$	$6.6^{+1.1}_{-1.4}$	$-1.9^{+0.5}_{-0.8}$	0.66 ± 0.03	0.5 ± 0.2	8020^{+30}_{-20}	680
SN 2019pud	0.6 ± 0.3	1.8 ± 0.5	6.2 ± 1.3	$-2.0^{+0.6}_{-0.7}$	$0.51^{+0.04}_{-0.02}$	0.8 ± 0.4	15000^{+600}_{-1100}	7.8
CSI fit	$\log f_{\rm Ni}$	$\log M_{\rm CSM}$ ($M_\odot$)	$\log M_{\rm ej}$ ($M_\odot$)	$\log R_0$ (au)	$\log \rho$ (g cm^{-3})	$v_{\rm ej}$ (km s^{-1})	E_k (10^{51} erg)	Score
SN 2019uba (s = 2)	$-2.6^{+0.7}_{-0.3}$	$1.1^{+0.2}_{-0.4}$	$-0.2^{+0.9}_{-0.5}$	$2.5^{+0.3}_{-0.4}$	-13 ± 1	11000^{+700}_{-900}	$0.4^{+3.1}_{-0.3}$	68.9
SN 2019uba (s = 0)	-1.9 ± 0.2	0.83 ± 0.06	$1.1^{+0.1}_{-0.2}$	2.2 ± 0.1	-12.4 ± 0.2	10000 ± 400	8 ± 2	72.0

7.2 Power sources

Previous studies on SLSNe II have suggested different mechanisms at work. Miller et al. (2009) favoured CSI with an opaque ejected shell as the dominant power source of SN 2008es, while Inserra et al. (2018), with a sample of three SLSNe II, suggested that a magnetar central engine is a good match to their light curves and temperatures. Bhirombhakdi et al. (2019) found the magnetar scenario to overpredict late-time fluxes of SN 2008es and unable to explain a NIR excess. They thus favoured the CSI model, but could not rule out a magnetar with a declining fraction of trapped energy. We note that both Inserra et al. (2018) and Bhirombhakdi et al. (2019) used the bolometric light curve for their fits, while MOSFIT (Guillochon et al. 2018) makes use of the colour information in the fitting as well. Even so, we find that the CSI and magnetar models included in MOSFIT are able to fit the light curves roughly equally well. ^{56}Ni decay as the dominant power source can be ruled out, but from light curves alone it is difficult to distinguish between CSI and magnetar models. A similar conclusion was reached by Chen et al. (2022b) for a large sample of SLSNe I from ZTF. Additionally, a few objects with UV data are not reproduced by MOSFIT.

Some of the CSI results in Tables 8 and 9, at face value, require exotic or implausible scenarios. For example, in the $s = 2$ case, SNe 2019aanx and 2019zcr have a CSM of tens of $M_\odot$ and much more massive than the ejecta, requiring mass loss rates on the order of 0.1 or 1 $M_\odot$ yr^{-1} depending on the wind velocity (i.e. an eruption, even if the density structure is $\propto \rho^{-2}$), and possibly fallback on to a nascent black hole resulting in a small ejecta mass. Meanwhile, a ^{56}Ni mass of $>10\,M_\odot$ is obtained for SN 2019uba with both s values. While large ejecta masses themselves are plausible in e.g. pulsational pair instability SNe (PPISNe), ^{56}Ni masses $\gtrsim 4M_\odot$ likely require bonafide PISNe (Kasen, Woosley & Heger 2011; Woosley 2017).

There are, however, other observational indications in favour of CSI. As noted in Section 5, it is possible that the model of Chatzopoulos et al. (2013) used in MOSFIT is too simplified to account for all the light curves, and a CSI power source should not be discarded based on the light-curve modelling. For example, more detailed numerical models by Sorokina et al. (2016) produce very different light curves than the Chatzopoulos et al. (2013) model. It may be more fruitful to try to exclude the magnetar model: for SNe 2019cqc and 2019pud, we obtain high ^{56}Ni masses of $\sim$2.5 and $\sim$0.9 $M_\odot$, respectively. We have, however, re-run both cases with $f_{\rm Ni} < 0.05$, and find fits of reasonable quality (by eye) without such high Ni masses. We have also re-run the CSI models for SN 2019uba, with a similar outcome. Thus the MOSFIT parameters should be treated with caution. We list the resulting parameters in Table 12.

The first indication of CSI comes from the UV photometry. As described in Section 4.4, in four of the six SNe where an SED with UV data can be constructed, we observe an excess over a blackbody function in the UV. This was also seen in e.g. SN 1979C (Panagia et al. 1980), SN 2008es (Miller et al. 2009), and SN 2010jl (Fransson et al. 2014). A forest of UV emission lines in SN 1979C was interpreted by Fransson et al. (1984) as being powered by excitation by X-rays from CSI. In spectra of SLSNe I, which are mostly consistent with the magnetar model, the UV spectrum is instead heavily blanketed by absorption lines (e.g. Yan et al. 2017, 2018). Additionally, absorption lines in SLSNe II are relatively weak compared to SNe II-P. Branch et al. (2000) attribute this to an additional contribution to the continuum emission from above the absorption layer, called 'top-lighting'. Such a scenario is better explained in the CSI model, as the central engine power source would necessarily be located below the absorption layer instead. Models by e.g. Dessart & Hillier (2022) also indicate both weakening absorption and increasing UV luminosity with increasing interaction power. The line profiles we observe, especially in the brighter, more 08es-like SNe, can be explained through CSI as well (see below).

We note, however, that in the CSI scenario, the energy source is ultimately the kinetic energy of the ejecta. The neutrino-driven explosion mechanism may have problems with kinetic energies of more than a few $\times$ 10^{51} erg (Janka 2012). According to the estimated UV-to-optical radiated energies (see Table 3), the explosion energies of the bright, 08es-like SNe must be $\gtrsim 10^{51}$ (SN 2019aanx), $\gtrsim 2 \times 10^{51}$ (SN 2019uba), or even $\gtrsim 3 \times 10^{51}$ (SN 2019zcr) even with a 100 per cent conversion efficiency. Note that as these estimates were not extrapolated into unobserved epochs and wavelengths, the true radiated energy is larger still.

The brightest SNe in the sample may thus need both CSI *and* a central engine – magnetar spin-down or possibly fallback accretion on to a black hole (Dexter & Kasen 2013). A similar problem was noted by Terreran et al. (2017) for the extremely energetic OGLE-2014-SN-073. Even in a PPISN scenario, more than 5×10^{51} erg of kinetic energy becomes a problem without a magnetar (Woosley 2017). More detailed studies will be necessary to constrain the contribution and nature of this additional power source. This can be done through e.g. late-time radio follow-up and possible detections of young pulsar wind nebulae (Omand, Kashiyama & Murase 2018; Law et al. 2019; Eftekhari et al. 2021). The kinetic energies from the CSI models, estimated as $E_k = 0.3 M_{ej} v_{ej}^2$, also often reach $>3 \times 10^{51}$ erg (see Tables 8 and 9), tentatively suggesting an additional power source as well; but the uncertainties are often large enough to allow $<2 \times 10^{51}$ erg. Only three SNe (not including the SN with the highest radiated energy, SN 2019zcr!) require $E_k > 3 \times 10^{51}$ erg in *both* the $s = 0$ and $s = 2$ models when uncertainties are taken into account.

Finally, we point out that SN 2020hgr, the slowest-evolving SN in our sample (see Section 4), is superficially similar to some PISN models. Kasen et al. (2011) showed that spectra of PISNe with hydrogen-rich 150–250 $M_\odot$ progenitors can also look similar to

those of normal SNe II and SN 2020hgr. However, the light curves of such models quickly rise to a plateau phase and/or have a main peak at hundreds of days post-explosion. PISNe from 80 to 100 $M_\odot$ helium stars do photometrically resemble that of SN 2020hgr, but the spectrum of SN 2020hgr is hydrogen-dominated until late times, while CCSNe with very small hydrogen masses (Type IIb) eventually develop strong helium features. These models tentatively argue against a PISN scenario, but do not rule it out entirely.

7.3 Line profiles and CSM structure

Taddia et al. (2020) modelled the line profile in SN 2013L, a SN IIn which exhibited both narrow/intermediate and broad Hα components. They showed that the shape of the broad component can be reproduced with a spherically symmetric CSM shell. A cool, dense shell (CDS) forms between the forward and reverse shocks (Chevalier & Fransson 1994, 2017). Broad emission lines would originate behind the radiative forward shock and would, without electron scattering, result in a boxy profile. However, Taddia et al. (2020) showed that a high optical depth for electron scattering (τ_e) in the unshocked, ionized CSM, combined with occultation of the receding side, would produce an emission profile with red-wing suppression but no broad P Cygni absorption, similar to what is seen in most SLSNe II. As τ_e increases further, this profile would become symmetric, as seen in the brightest SLSNe II.

The narrow/intermediate line profile in such a scenario originates in the ionized, unshocked CSM that is also responsible for the electron scattering. If τ_e is high enough ($\gtrsim$30), the existence of a non-dominant narrow electron scattering component such as in SN 2013L, even if easily visible in emission at a lower τ_e, can be hidden (Taddia et al. 2020). In the case of an asymmetric line profile and lower τ_e, the narrow emission component must be intrinsically weak. A low density in the unshocked region would result in a weak narrow component – requiring an extended ionized CSM. A weak narrow feature, or a narrow P Cygni profile from optically thin outer CSM, may escape detection without high-resolution spectra, as seen e.g. in SNe 2010jl and the very similar 2015da at late times (Zhang et al. 2012; Fransson et al. 2014; Tartaglia et al. 2020). Stronger interaction would result in both a more luminous SN and simultaneously a higher τ_e, as any extended CSM would be ionized further out.

Late-time multicomponent Hα profiles were seen in PS15br and SN 2013hx (Inserra et al. 2018); they can in principle result from the shell interaction described above (Taddia et al. 2020). However, one component in this case is the smeared-out narrow profile, whereas in PS15br a narrow P Cygni feature was not seen even in high-resolution spectra, making this scenario unlikely, and SN 2013hx showed a three-component profile. They thus likely still require asymmetric CSM, but for our SNe, which lack such line profiles at late times, this is not necessary. The lack of strong forbidden metal lines in late-time spectra can simply be due to not being truly nebular at $\lesssim$+300 d. The density at the emitting region is still high enough that atoms/ions are collisionally de-excited instead of emitting in forbidden lines. The red wing is often suppressed, implying occultation of the far side – this also argues that the spectra are not nebular. Longer follow-up campaigns are needed to study SLSNe II in the nebular phase.

The scenario described above may not be required for all SLSNe II. Some show P Cygni profiles in Hα similar to less luminous SNe II (or, for SN 2019pud, no clear absorption trough but a suppressed blue wing, presumably also from absorption in H-rich ejecta), which indicate a line of sight into the ejecta and are not expected to be seen through an optically thick CDS. In SN 2020yue, this is seen very early. A clumpy CDS can result in optically thin gaps in the CDS (Smith et al. 2008), but it is also possible that the CSM is overrun by the ejecta in an early stage, e.g. if the CSM is disc-shaped (McDowell et al. 2018).

Moriya & Tominaga (2012) proposed a model in which the forward shock breaks out of an optically thick shell or wind CSM, resulting in a broadened light curve peak. At early times, this results in a blue, featureless spectrum, followed by the broad emission lines post-peak. If the outer layers of the CSM are optically less thick, they would be unshocked but ionized and result in a SN IIn, while a SN II-L could result if the CSM density is roughly constant: very little unshocked CSM remains after this breakout and photons originate from the shocked CSM and the ejecta. We do not see early bumps in our light curves (see Figs 9 and 10) similar to what e.g. Angus et al. (2019) observe in some SLSNe I, possibly associated with shock cooling and an extended progenitor. In most cases, we cannot exclude them either, but their absence is consistent with the main peak being associated with a breakout from the CSM shell. A similar scenario has been proposed for normal SNe II (Förster et al. 2018).

A combination of effects may be at play. The brightest SLSNe II with broad symmetric emission, and possibly others, can be explained through electron scattering in the unshocked CSM. A range of τ_e values can produce different Hα lines, symmetric profiles with a very high τ_e and profiles similar to SN 2019gsp or SN 2020bfe possibly with a somewhat lower τ_e. Other SLSNe II, such as SN 2020hgr, which seem to require CSI based on its UV excess but whose spectrum is extremely similar to SNe II-L, may require dense CSM confined to small radii, possibly in a disc shape. Normal wind mass loss ($\lesssim 10^{-6}$ $M_\odot$ yr^{-1} in RSGs according to Beasor et al. 2020) would not significantly contribute to the emission.

CSI has been argued to be required in the early epochs of many if not all SNe II (Morozova et al. 2018); its signatures can be seen in the radio light curves of SNe II-L (Lundqvist & Fransson 1988) and in the UV spectrum of SN 1979C (Fransson et al. 1984). An increasing amount of CSM can result in light curves with shorter plateaus and brighter, broader peaks (Moriya et al. 2011), even including absolute magnitudes of $\sim$−22 mag for pre-SN mass loss rates $\gtrsim$0.1 $M_\odot$ yr^{-1}. We thus suggest a continuum of recent mass loss from SNe II-P through SNe II-L to some SLSNe II. At least the SNe spectroscopically similar to SN 2008es seem to additionally require a more extended CSM and thus may be a separate group. Detailed numerical modelling of SLSNe II to determine the properties of the CSM is outside the scope of this study.

7.4 Clues on SLSN II progenitors

As stated in Section 2, our sample criteria are matched by 14 of the 69 hydrogen-rich SLSNe followed up in the ZTF phase I. This would imply a fraction of $0.20^{+0.05}_{-0.06}$ (Gehrels 1986) out of all hydrogen-rich SNe with $M_g < -20$ mag having broad emission lines without narrow ones. However, as we point out in Section 4.3, there is some overlap in photometric properties between SLSNe II and IIn in ZTF. It is possible, as stated in Section 2, that since some SLSNe IIn in ZTF only have pre-peak spectra, broad lines might have appeared later and replaced the earlier narrow lines (and the latter may in rare cases be from the host). Therefore the fraction should be considered a lower limit: SNe similar to our sample make up >14 per cent of the transients classified as SLSNe II by ZTF. If spectroscopically 08es-like SNe, i.e. those with the highest τ_e and strongest interaction, are considered separately, we can similarly imply a fraction of 3/69, i.e. 0.04 ± 0.03. This should again be considered a lower limit, i.e. >1 per cent. This is in line with the rarity of such SNe in the literature even compared to other SLSNe (Inserra et al. 2018).

The properties of the progenitor systems of these SNe – i.e. mass loss history and initial mass – must be unusual, even for SLSNe. The mass-loss history can be affected by a binary companion, the metallicity of the progenitor and/or its initial mass (e.g. Smith 2014). Although light curves alone cannot rule out magnetars, our results indicate that CSI is required by most if not all SLSNe II; SLSNe IIn, on the other hand, are clearly primarily powered by CSI. If CSI is responsible for both, the density profile of the CSM and thus mass-loss history must be different – but weaker narrow emission lines or narrow P Cygni profiles can escape detection without high-resolution spectra. The host galaxies of SLSNe II are quite similar to those of SLSNe IIn (see Section 6), which suggests that their environments and metallicities are similar as well (but our sample size remains rather small). In such a case a difference in progenitor mass and/or a binary companion could be causing the different mass-loss histories of SLSNe II and IIn. In the Moriya & Tominaga (2012) and Taddia et al. (2020) models, an asymmetric CSM is not required. Instead of (or in addition to) mass loss through binary interaction, the ejection of a spherically symmetric shell in an eruption close to the death of the progenitor star may result in the dense CSM that would produce the observed line profiles.

Eruptive mass loss seems to be necessary even in many normal SNe II, where CSM masses may reach $\gtrsim 0.5\,M_\odot$ (Morozova et al. 2018) and CSM radii have been argued to be on the order of $1000\,R_\odot$, i.e. not much larger than the progenitors themselves. Moriya et al. (2011) also suggested strong mass loss in RSGs and yellow supergiants (YSGs) just before their deaths. In SLSNe IIn, on the other hand, a longer-lasting, strong wind or a series of eruptive events (such as pulsational pair instability; Woosley, Blinnikov & Heger 2007) may be responsible for a more extended dense CSM. A possible mechanism for eruptions in the very late stages of RSG evolution is the so-called wave-driven mass loss (Quataert & Shiode 2012; Shiode & Quataert 2014), which can unbind up to $\sim 10\,M_\odot$ in the last months or years before explosion after carbon-burning

The progenitors of normal SNe II-P are established as RSGs of roughly 8–17 $M_\odot$ (Smartt 2009), while the progenitors of SNe II-L are less well-known, but consistent with initial masses of 15–20 $M_\odot$ (van Dyk et al. 1999; Faran et al. 2014; Kangas et al. 2016, 2017). Very massive luminous blue variable stars, on the other hand, are connected to SNe IIn (e.g. Smith et al. 2010, 2011; Mauerhan et al. 2013; Taddia et al. 2013; Fransson et al. 2014). If SNe II-P, II-L and some SLSNe II are connected by a continuum of increasing mass lost through a similar eruptive mechanism, the rare progenitors of the latter may be the most massive RSGs or YSGs. The diversity within the sample may indicate multiple progenitor scenarios, though. Other SLSNe II, including those similar to SN 2008es, may require a more extended, low-density CSM as the location of electron scattering. Based on our host galaxy modelling, the 08es-like SNe – which may require central engines as well as CSI – may also favour lower metallicities than the rest, which is the case for SLSNe I where magnetar engines are the most popular scenario (Perley et al. 2016; Schulze et al. 2018).

8 SUMMARY AND CONCLUSIONS

We have examined the light curves and spectra of a sample of 14 SLSNe II from ZTF phase I that exhibit broad Balmer-line emission without strong narrow lines typical to (SL)SNe IIn. This is the largest such sample to date. We have used light-curve models to attempt to constrain the power sources responsible for the luminosity of SLSNe II. Based on this work, we draw the following conclusions.

(i) The spectra of several SLSNe II are very similar to those of SNe II-L. Broad, asymmetric Balmer-line emission is accompanied by weak or non-existent P Cygni absorption and metal lines typical to SNe II. Photometrically, these SLSNe evolve slower than normal SNe II-L and do not clearly exhibit the typical plateau/bump phase followed by a drop to ^{56}Co decay tail, instead resembling SLSNe I.

(ii) Other SLSNe II include three very luminous ($M_g \leq -21.7$ mag, even -22.6 mag, at peak and requiring at least 10^{51} erg in radiated energy) SNe that resemble the prototypical event SN 2008es more than normal SNe II. Hα emission is symmetric until late times and absorption lines are weak. A close resemblance to SN 2008es is, however, far from ubiquitous among SLSNe II. The sample also includes two fast-declining SNe that exhibit spectroscopic features not present in the two aforementioned groups.

(iii) Light-curve models invoking a magnetar engine (Kasen & Bildsten 2010) or CSI (Chatzopoulos et al. 2013) are roughly equally successful in reproducing the observed evolution, and some SLSNe II with UV observations are difficult for both. Only a pure ^{56}Ni-powered model can be excluded.

(iv) However, we observe an excess in the UV compared to a blackbody in several cases, including a wide range of photometric and spectral properties, which is likely due to a forest of emission lines from various species ionized by X-rays from CSI. At least these SNe seem to be CSM-powered. It is also possible, however, that the extreme radiated energies of the brightest SLSNe II, $\gtrsim 2 \times 10^{51}$ or even $\gtrsim 3 \times 10^{51}$ erg, require a central engine as well as CSI.

(v) The emission lines of the brightest, 08es-like SLSNe II can be explained through interaction with a dense CSM, observed through a screen of ionized, unshocked CSM optically thick to electron scattering. SLSNe II spectroscopically more similar to normal SNe II may involve a dense CSM confined to small radii of the progenitor star. Eruptive mass loss has been argued to be important in SNe II, especially II-L; thus some SLSNe II may be connected to normal SNe II through a continuum of pre-SN mass loss.

(vi) SLSNe II without narrow emission lines comprise roughly 20 per cent of all hydrogen-rich SLSNe followed up by ZTF. This rarity even compared to other SLSNe indicates highly unusual progenitor stars and/or mass-loss histories. The host galaxies of SLSNe II strongly overlap with those of SLSNe IIn, indicating a similar environment; differences in mass-loss history may thus be connected to initial mass rather than metallicity.

(vii) All observed late-time spectra of SLSNe II, including SN 2013hx and PS15br (Inserra et al. 2018), lack strong forbidden metal lines typical to normal SNe II at similar phases; these SNe are likely not yet nebular at $\sim$+300 d. No multicomponent line profiles similar to SN 2013hx and PS15br are seen in our sample, indicating that interaction with *asymmetric* CSM is not required by most late-time spectra.

ACKNOWLEDGEMENTS

We thank the anonymous referee for suggestions that helped to improve the paper.

This study is based on observations obtained with the Samuel Oschin Telescope 48-inch and the 60-inch Telescope at the Palomar Observatory as part of the ZTF project. ZTF is supported by the National Science Foundation under grants no. AST-1440341 and AST-2034437 and a collaboration including current partners Caltech, IPAC, the Weizmann Institute for Science, the Oskar Klein Center at Stockholm University, the University of Maryland, Deutsches Elektronen-Synchrotron and Humboldt University, the TANGO Consortium of Taiwan, the University of Wisconsin

at Milwaukee, Trinity College Dublin, Lawrence Livermore National Laboratories, IN2P3, University of Warwick, Ruhr University Bochum, Northwestern University and former partners the University of Washington, Los Alamos National Laboratories, and Lawrence Berkeley National Laboratories. Operations are conducted by COO, IPAC, and UW. SED Machine is based upon work supported by the National Science Foundation under grant no. 1106171. The ZTF forced-photometry service was funded under the Heising-Simons Foundation grant #12540303 (PI: Graham). This work uses the GROWTH Followup Marshal (Kasliwal et al. 2019) and was supported by the GROWTH project funded by the National Science Foundation under grant no. 1545949.

This study is based partially on observations made with the NOT, owned in collaboration by the University of Turku and Aarhus University, and operated jointly by Aarhus University, the University of Turku, and the University of Oslo, representing Denmark, Finland, and Norway, the University of Iceland and Stockholm University at the Observatorio del Roque de los Muchachos, La Palma, Spain, of the Instituto de Astrofísica de Canarias. The data presented here were obtained in part with ALFOSC, which is provided by the Instituto de Astrofísica de Andalucia (IAA) under a joint agreement with the University of Copenhagen and NOT. The LT is operated on the island of La Palma by Liverpool John Moores University in the Spanish Observatorio del Roque de los Muchachos of the Instituto de Astrofísica de Canarias with financial support from the UK Science and Technology Facilities Council. The WHT is operated on the island of La Palma by the Isaac Newton Group of Telescopes in the Spanish Observatorio del Roque de los Muchachos of the Instituto de Astrofísica de Canarias.

Some of the data presented herein were obtained at the W. M. Keck Observatory, which is operated as a scientific partnership among the California Institute of Technology, the University of California, and the National Aeronautics and Space Administration. The Observatory was made possible by the generous financial support of the W. M. Keck Foundation. The authors wish to recognize and acknowledge the very significant cultural role and reverence that the summit of Maunakea has always had within the indigenous Hawaiian community. We are most fortunate to have the opportunity to conduct observations from this mountain.

TK acknowledges support from the Swedish National Space Agency and the Swedish Research Council. SS acknowledges support from the Gravitational Radiation and Electromagnetic Astrophysical Transients (GREAT) research environment, funded by Vetenskapsrådet, the Swedish Research Council, project number 2016-06012. RL acknowledges support from a Marie Skłodowska-Curie Individual Fellowship within the Horizon 2020 European Union (EU) Framework Programme for Research and Innovation (H2020- MSCA-IF-2017-794467). TWC acknowledges EU funding under Marie Skłodowska-Curie grant H2020-MSCA-IF-2018-842471. LT acknowledges support from Ministero dell'Istruzione (MIUR); Progetti di Ricerca di Interesse Nazionale (PRIN) 2017 grant 20179ZF5KS. AGY's research is supported by the EU via European Research Council (ERC) grant no. 725161, the Israel Science Foundation (ISF) gravitational wave (GW) excellence center, an Isreal Ministry of Science (IMOS) space infrastructure grant and Binational Science Foundation (BSF)/Transformative and Global Innovation Fund (GIF) grants, as well as the André Deloro Institute for Advanced Research in Space and Optics, the Schwartz/Reisman Collaborative Science Program and the Norman E Alexander Family M Foundation ULTRASAT Data Center Fund, The Kimmel center for Planetary Sciences, Minerva and Yeda-Sela; AGY is the incumbent of the The Arlyn Imberman Professorial Chair.

DATA AVAILABILITY

The photometry data used in this study are included as supplementary material; raw images used in ZTF photometry are publicly available through ZTF Data Release 10 at https://www.ztf.caltech.edu/ztf-public-releases.html. All output corner plot files and figures from light-curve modelling are also included as supplementary material. Reduced spectra used in this study are publicly available through WISEREP (https://www.wiserep.org/). The derived data generated in this research will be shared on reasonable request to the corresponding author.

Optical/UV *Swift* photometry data used in this paper are available publicly on the NASA Swift Data Archive (https://heasarc.gsfc.nasa.gov/). X-ray count rates are publicly available on *Swift* XRT website (https://www.swift.ac.uk/user_objects/). Similarly, the host galaxy data used in this paper were obtained from public data repositories as described in Section 6.

REFERENCES

Ahn C. P. et al., 2012, ApJS, 203, 21
Ambikasaran S., Foreman-Mackey D., Greengard L., Hogg D. W., O'Neil M., 2015, IEEE Transact. Patt. Anal. Mach. Intell., 38, 252
Anderson J. P. et al., 2014, ApJ, 786, 67
Angus C. R. et al., 2019, MNRAS, 487, 2215
Arnett W. D., 1982, ApJ, 253, 785
Barbon R., Ciatti F., Rosino L., 1979, A&A, 72, 287
Barkat Z., Rakavy G., Sack N., 1967, Phys. Rev. Lett., 18, 379
Barnsley R. M., Smith R. J., Steele I. A., 2012, Astron. Nachr., 333, 101
Beasor E. R., Davies B., Smith N., van Loon J. T., Gehrz R. D., Figer D. F., 2020, MNRAS, 492, 5994
Bellm E. C., Sesar B., 2016, Astrophysics Source Code Library. record ascl:1602.002
Bellm E. C. et al., 2019a, PASP, 131, 018002
Bellm E. C. et al., 2019b, PASP, 131, 068003
Benetti S. et al., 2014, MNRAS, 441, 289
Bennett C. L., Larson D., Weiland J. L., Hinshaw G., 2014, ApJ, 794, 135
Bhirombhakdi K., Chornock R., Miller A. A., Filippenko A. V., Cenko S. B., Smith N., 2019, MNRAS, 488, 3783
Blagorodnova N. et al., 2018, PASP, 130, 035003
Blinnikov S. I., Bartunov O. S., 1993, A&A, 273, 106
Bose S. et al., 2018, ApJ, 862, 107
Branch D., Nomoto K., Filippenko A. V., 1991, Comments Astrophys., 15, 221
Branch D., Jeffery D. J., Blaylock M., Hatano K., 2000, PASP, 112, 217
Breeveld A. A., Landsman W., Holland S. T., Roming P., Kuin N. P. M., Page M. J., 2011a, in McEnery J. E., Racusin J. L., Gehrels N., eds, AIP Conf. Ser. Vol. 1358, Gamma Ray Bursts 2010. Am. Inst. Phys., New York, p. 373
Breeveld A. A., Landsman W., Holland S. T., Roming P., Kuin N. P. M., Page M. J., 2011b, in McEnery J. E., Racusin J. L., Gehrels N., eds, American Institute of Physics Conference Series Vol. 1358, Gamma Ray Bursts 2010. Am. Inst. Phys., New York, p. 373
Bressan A., Marigo P., Girardi L., Salasnich B., Dal Cero C., Rubele S., Nanni A., 2012, MNRAS, 427, 127
Bruch R. J. et al., 2021, ApJ, 912, 46
Calzetti D., Armus L., Bohlin R. C., Kinney A. L., Koornneef J., Storchi-Bergmann T., 2000, ApJ, 533, 682
Cardelli J. A., Clayton G. C., Mathis J. S., 1989, ApJ, 345, 245
Chandra P., Chevalier R. A., Chugai N., Fransson C., Soderberg A. M., 2015, ApJ, 810, 32
Chatzopoulos E., Wheeler J. C., Vinko J., Horvath Z. L., Nagy A., 2013, ApJ, 773, 76
Chen T. W. et al., 2015, MNRAS, 452, 1567
Chen T. W. et al., 2017, A&A, 602, A9

Chen Z. H. et al., 2022a, preprint (arXiv:2202.02059)
Chen Z. H. et al., 2022b, preprint (arXiv:2202.02060)
Chevalier R. A., Fransson C., 1994, ApJ, 420, 268
Chevalier R. A., Fransson C., 2017, in Alsabti A. W., Murdin P., eds, Handbook of Supernovae. Springer International Publishing AG, New York, p. 875
Chugai N. N., Utrobin V. P., 2022, MNRAS, 512, L71
Conroy C., Gunn J. E., White M., 2009, ApJ, 699, 486
Cutri R. M. et al., 2013, Technical report, Explanatory Supplement to the AllWISE Data Release Products
Davies B., Figer D. F., Kudritzki R.-P., Trombley C., Kouveliotou C., Wachter S., 2009, ApJ, 707, 844
De Cia A. et al., 2018, ApJ, 860, 100
de Vaucouleurs G., de Vaucouleurs A., Buta R., Ables H. D., Hewitt A. V., 1981, PASP, 93, 36
Dekany R. et al., 2020, PASP, 132, 038001
Dessart L., Hillier D. J., 2020, A&A, 642, A33
Dessart L., Hillier D. J., 2022, A&A, 660, L9
Dessart L., Audit E., Hillier D. J., 2015, MNRAS, 449, 4304
Dexter J., Kasen D., 2013, ApJ, 772, 30
Dey A. et al., 2019, AJ, 157, 168
Dong S. et al., 2016, Science, 351, 257
Eftekhari T., Margalit B., Omand C. M. B. et al., 2021, ApJ, 912, 21
Elmhamdi A. et al., 2003, MNRAS, 338, 939
Faran T. et al., 2014, MNRAS, 445, 554
Fassia A. et al., 2000, MNRAS, 318, 1093
Fassia A. et al., 2001, MNRAS, 325, 907
Foreman-Mackey D., Sick J., Johnson B., 2014, Python-Fsps: Python Bindings To Fsps (V0.1.1), Zenodo
Förster F. et al., 2018, Nature Astron., 2, 808
Fransson C., Benvenuti P., Gordon C., Hempe K., Palumbo G. G. C., Panagia N., Reimers D., Wamsteker W., 1984, A&A, 132, 1
Fransson C. et al., 2014, ApJ, 797, 118
Fremling C. et al., 2016, A&A, 593, A68
Fremling C. et al., 2020, ApJ, 895, 32
Gaensler B. M., McClure-Griffiths N. M., Oey M. S., Haverkorn M., Dickey J. M., Green A. J., 2005, ApJ, 620, L95
Gal-Yam A., 2012, Science, 337, 927
Gal-Yam A., 2019, ARA&A, 57, 305
Gal-Yam A. et al., 2022, Nature, 601, 201
Gehrels N., 1986, ApJ, 303, 336
Gezari S. et al., 2009, ApJ, 690, 1313
Gomez S., Berger E., Nicholl M., Blanchard P. K., Hosseinzadeh G., 2022, preprint (arXiv:2204.08486)
González-Gaitán S. et al., 2015, MNRAS, 451, 2212
Graham M. J. et al., 2019, PASP, 131, 078001
Guillochon J., Nicholl M., Villar V. A., Mockler B., Narayan G., Mandel K. S., Berger E., Williams P. K. G., 2018, ApJS, 236, 6
Güver T., Özel F., 2009, MNRAS, 400, 2050
Hamuy M. et al., 2003, Nature, 424, 651
Heger A., Woosley S. E., 2002, ApJ, 567, 532
Heger A., Woosley S. E., Spruit H. C., 2005, ApJ, 626, 350
Hogg D. W., Baldry I. K., Blanton M. R., Eisenstein D. J., 2002, preprint (arXiv:astro–ph/0210394)
Hosseinzadeh G., Berger E., Metzger B. D., Gomez S., Nicholl M., Blanchard P., 2022, ApJ, 933, 14
Inserra C. et al., 2013a, A&A, 555, A142
Inserra C. et al., 2013b, ApJ, 770, 128
Inserra C. et al., 2017, MNRAS, 468, 4642
Inserra C. et al., 2018, MNRAS, 475, 1046
Janka H.-T., 2012, Annu. Rev. Nucl. Part. Sci., 62, 407
Jerkstrand A. et al., 2017, ApJ, 835, 13
Jiang B., Jiang S., Ashley Villar V., 2020, Res. Notes Am. Astron. Soc., 4, 16
Kangas T. et al., 2016, MNRAS, 456, 323
Kangas T. et al., 2017, A&A, 597, A92
Kankare E. et al., 2017, Nature Astron., 1, 865
Karamehmetoglu E. et al., 2021, A&A, 649, A163
Kasen D., Bildsten L., 2010, ApJ, 717, 245
Kasen D., Woosley S. E., Heger A., 2011, ApJ, 734, 102
Kasliwal M. M. et al., 2019, PASP, 131, 038003
Khazov D. et al., 2016, ApJ, 818, 3
Kool E. C. et al., 2021, A&A, 652, A136
Lang D., 2014, AJ, 147, 108
Law C. J. et al., 2019, ApJ, 886, 24
Lee N. et al., 2015, ApJ, 801, 80
Leja J., Johnson B. D., Conroy C., van Dokkum P. G., Byler N., 2017, ApJ, 837, 170
Leloudas G. et al., 2016, Nature Astron., 1, 0002
Leonard D. C., Filippenko A. V., Barth A. J., Matheson T., 2000, ApJ, 536, 239
Li L., Dai Z.-G., Wang S.-Q., Zhong S.-Q., 2020, ApJ, 900, 121
Lundqvist P., Fransson C., 1988, A&A, 192, 221
Lunnan R. et al., 2018, Nature Astron., 2, 887
Mainzer A. et al., 2014, ApJ, 792, 30
Martin D. C. et al., 2005, ApJ, 619, L1
Masci F. J. et al., 2019, PASP, 131, 018003
Mauerhan J. C. et al., 2013, MNRAS, 430, 1801
McDowell A. T., Duffell P. C., Kasen D., 2018, ApJ, 856, 29
Meisner A. M., Lang D., Schlegel D. J., 2017, AJ, 153, 38
Miller A. A. et al., 2009, ApJ, 690, 1303
Moriya T. J., Tominaga N., 2012, ApJ, 747, 118
Moriya T., Tominaga N., Blinnikov S. I., Baklanov P. V., Sorokina E. I., 2011, MNRAS, 415, 199
Moriya T. J., Sorokina E. I., Chevalier R. A., 2018, Space Sci. Rev., 214, 59
Moriya T. J., Murase K., Kashiyama K., Blinnikov S. I., 2022, MNRAS, 513, 6210
Morozova V., Piro A. L., Valenti S., 2018, ApJ, 858, 15
Nadyozhin D. K., 1994, ApJS, 92, 527
Nagy A. P., 2018, ApJ, 862, 143
Nicholl M. et al., 2013, Nature, 502, 346
Nicholl M. et al., 2015, MNRAS, 452, 3869
Nicholl M., Guillochon J., Berger E., 2017, ApJ, 850, 55
Ofek E. O. et al., 2007, ApJ, 659, L13
Oke J. B., Gunn J. E., 1982, PASP, 94, 586
Oke J. B., Gunn J. E., 1983, ApJ, 266, 713
Oke J. B. et al., 1995, PASP, 107, 375
Olausen S. A., Kaspi V. M., 2014, ApJS, 212, 6
Omand C. M. B., Kashiyama K., Murase K., 2018, MNRAS, 474, 573
Panagia N. et al., 1980, MNRAS, 192, 861
Peng C. Y., Ho L. C., Impey C. D., Rix H.-W., 2010, AJ, 139, 2097
Perley D. A., 2019, PASP, 131, 084503
Perley D. A. et al., 2016, ApJ, 830, 13
Perley D. A. et al., 2020, ApJ, 904, 35
Podsiadlowski P., 1992, PASP, 104, 717
Prochaska J. et al., 2020, J. Open Sour. Softw., 5, 2308
Quataert E., Shiode J., 2012, MNRAS, 423, L92
Quimby R. M. et al., 2011, Nature, 474, 487
Quimby R. M. et al., 2018, ApJ, 855, 2
Rasmussen C. E., Williams C. K. I., 2006, Gaussian Processes for Machine Learning. Adaptive Computation and Machine Learning. MIT Press, Cambridge, MA
Reynolds T. M. et al., 2020, MNRAS, 493, 1761
Rigault M. et al., 2019, A&A, 627, A115
Roberson M. S., Fremling C., Kasliwal M. M., 2022, J. Open Sour. Softw., 7, 3612
Schlafly E. F., Finkbeiner D. P., 2011, ApJ, 737, 103
Schulze S. et al., 2018, MNRAS, 473, 1258
Schulze S. et al., 2021, ApJS, 255, 29
Shibata M., Zhou E., Kiuchi K., Fujibayashi S., 2019, Phys. Rev. D, 100, 023015
Shiode J. H., Quataert E., 2014, ApJ, 780, 96
Smartt S. J., 2009, ARA&A, 47, 63
Smith N., 2014, ARA&A, 52, 487
Smith N. et al., 2007, ApJ, 666, 1116
Smith N., Chornock R., Li W., Ganeshalingam M., Silverman J. M., Foley R. J., Filippenko A. V., Barth A. J., 2008, ApJ, 686, 467
Smith N. et al., 2010, AJ, 139, 1451
Smith N. et al., 2011, ApJ, 732, 63

Sorokina E., Blinnikov S., Nomoto K., Quimby R., Tolstov A., 2016, ApJ, 829, 17
Steele I. A. et al., 2004, in Oschmann J. M., Jr, ed., Proc. SPIE Conf. Ser. Vol. 5489, Ground-Based Telescopes. SPIE, Bellingham, p. 679
Stevance H. F., Eldridge J. J., 2021, MNRAS, 504, L51
Taddia F. et al., 2013, A&A, 555, A10
Taddia F. et al., 2020, A&A, 638, A92
Taggart K., 2020, PhD thesis, Liverpool John Moores University
Tartaglia L. et al., 2020, A&A, 635, A39
Tartaglia L. et al., 2021, ApJ, 907, 52
Terreran G. et al., 2016, MNRAS, 462, 137
Terreran G. et al., 2017, Nature Astron., 1, 713
Tody D., 1986, in Crawford D. L., ed., Proc. SPIE Conf. Ser. Vol. 627, Instrumentation in Astronomy VI. SPIE, Bellingham, p. 733
Turatto M., Cappellaro E., Danziger I. J., Benetti S., Gouiffes C., della Valle M., 1993, MNRAS, 262, 128
Turatto M. et al., 2000, ApJ, 534, L57
Uomoto A., Kirshner R. P., 1986, ApJ, 308, 685
Valenti S. et al., 2015, MNRAS, 448, 2608
van Dyk S. D. et al., 1999, PASP, 111, 313
Villar V. A., Berger E., Metzger B. D., Guillochon J., 2017, ApJ, 849, 70
Watanabe S., 2010, Neural Netw., 23, 20
West S. L. et al., 2022, preprint (arXiv:2205.11143)
Woosley S. E., 2010, ApJ, 719, L204
Woosley S. E., 2017, ApJ, 836, 244
Woosley S. E., Blinnikov S., Heger A., 2007, Nature, 450, 390
Wright E. L. et al., 2010, AJ, 140, 1868
Wright A. H. et al., 2016, MNRAS, 460, 765
Yan L. et al., 2017, ApJ, 840, 57
Yan L., Perley D. A., De Cia A., Quimby R., Lunnan R., Rubin K. H. R., Brown P. J., 2018, ApJ, 858, 91
Yaron O., Gal-Yam A., 2012, PASP, 124, 668
Zackay B., Ofek E. O., Gal-Yam A., 2016, ApJ, 830, 27
Zhang T. et al., 2012, AJ, 144, 131

SUPPORTING INFORMATION

Supplementary data are available at *MNRAS* online.

supplementary.zip

Please note: Oxford University Press is not responsible for the content or functionality of any supporting materials supplied by the authors. Any queries (other than missing material) should be directed to the corresponding author for the article.

APPENDIX A: LOGS OF OBSERVATIONS

Full logs of all spectroscopic observations and optical and UV photometry (including upper limits) used in this study are available

Table A1. The first 10 lines of the log of spectroscopic observations used in this paper. The full table is available in supplementary material.

SN	Julian date (d)	Phase (d)	Telescope	Instrument	Exposure time (s)	Slit ″	Grism/grating
SN 2018jkq	2458462.700	−12	P60	SEDM	2250	IFU	-
SN 2018jkq	2458471.737	−4	P60	SEDM	1200	IFU	-
SN 2018jkq	2458472.776	−3	P60	SEDM	1200	IFU	-
SN 2018jkq	2458473.652	−2	P60	SEDM	1200	IFU	-
SN 2018jkq	2458479.615	3	P200	DBSP	600	2.0	600/4000 + 316/7500
SN 2018jkq	2458480.763	4	P60	SEDM	1200	IFU	-
SN 2018jkq	2458484.341	7	WHT	ISIS	800	1.5	R300B + R316R
SN 2018jkq	2458490.702	13	P200	DBSP	900	IFU	600/4000 + 316/7500
SN 2018jkq	2458667.051	170	Keck	LRIS	900	IFU	400/3400 + 400/8500
SN 2018lqi	2458762.858	−18	P200	DBSP	900	1.5	600/4000 + 316/7500

Table A2. The first 20 lines of the table of photometry used in this paper. The full table is available in supplementary material. An apparent magnitude of 99 denotes a non-detection.

SN	Julian date (d)	Filter	App. magnitude (mag)	Error (mag)	Upper limit (mag)	Instrument
SN2018jkq	2458426.7547	*r*	99	99	20.41	P48 + ZTF
SN2018jkq	2458426.8254	*g*	99	99	20.08	P48 + ZTF
SN2018jkq	2458427.7796	*i*	99	99	19.13	P48 + ZTF
SN2018jkq	2458427.7829	*i*	99	99	18.85	P48 + ZTF
SN2018jkq	2458429.7746	*r*	99	99	20.71	P48 + ZTF
SN2018jkq	2458431.7597	*i*	99	99	19.05	P48 + ZTF
SN2018jkq	2458431.7630	*i*	99	99	19.16	P48 + ZTF
SN2018jkq	2458432.7688	*r*	99	99	20.20	P48 + ZTF
SN2018jkq	2458435.7287	*g*	99	99	20.25	P48 + ZTF
SN2018jkq	2458435.7327	*i*	99	99	19.26	P48 + ZTF
SN2018jkq	2458435.7685	*r*	99	99	19.80	P48 + ZTF
SN2018jkq	2458438.8190	*r*	99	99	17.46	P48 + ZTF
SN2018jkq	2458438.8583	*g*	99	99	16.97	P48 + ZTF
SN2018jkq	2458441.7384	*g*	99	99	19.53	P48 + ZTF
SN2018jkq	2458441.7752	*r*	99	99	19.41	P48 + ZTF
SN2018jkq	2458447.8300	*r*	99	99	19.46	P48 + ZTF
SN2018jkq	2458450.7496	*r*	99	99	18.14	P48 + ZTF
SN2018jkq	2458450.7550	*g*	99	99	18.53	P48 + ZTF
SN2018jkq	2458450.8014	*r*	99	99	15.62	P48 + ZTF
SN2018jkq	2458456.6831	*r*	18.94	0.08	20.25	P48 + ZTF

as supplementary material. We present samples of these logs in Tables A1 and A2, respectively.

APPENDIX B: X-RAY LIMITS

We have obtained the count-rate limits for our targets on the *Swift* XRT website.[17] A total of nine SNe out of the sample have associated XRT observations after the discovery of the SN; these are listed in Table B1. No SLSN source was detected in these observations. We therefore list the upper limits in the table in terms of count rate and flux over the 0.2–10 keV band of XRT. Count rates were converted to fluxes using `WebPIMMS`,[18] assuming host hydrogen column density $n_{H,\,\mathrm{host}} = 2 \times 10^{21}$ erg (the least constraining case in our light-curve models; see Section 5.1) and an Astrophysical Plasma Emission Code model with a temperature of 19 keV, similar to the X-ray spectrum of SN 2010jl (Chandra et al. 2015). Galactic hydrogen column densities were obtained from the NASA HEASARC `nH` tool.[19]

The 3σ upper limits in the 0.2–10 keV range from the XRT archive are typically on the order of a few $\times\ 10^{-13}$ erg s^{-1} cm^{-2} or even higher, an order of magnitude less constraining than that determined for SN 2008es (Gezari et al. 2009). Depending on the target redshift, these translate into limits on the 0.2–10 keV luminosity between $\lesssim 10^{42}$ and $\lesssim 10^{44}$ erg s^{-1} (SN 2020jhm at 480 d and SN 2019zcr at <50 d, respectively). These limits are orders of magnitude higher than the observed luminosity of the strongly interacting, relatively nearby and almost superluminous SN 2010jl between 50 and 1300 d (Chandra et al. 2015), from 6×10^{39} to 1.3×10^{40} erg s^{-1}. Thus the X-ray non-detections do not exclude CSI as the dominant power source.

Table B1. Upper limits (3σ) of count rate and unabsorbed flux in the 0.2–10 keV band of XRT for sample SNe with associated X-ray observations. Epochs are relative to the rest-frame *g*-band peak.

SN	Epoch (d)	Count rate (10^{-3} ct s^{-1})	Flux (erg s^{-1} cm^{-2})
SN 2019kwr	733.5	<7.8	$<4.6 \times 10^{-13}$
SN 2019cqc	26.9	<3.4	$<2.2 \times 10^{-13}$
	40.5	<3.1	$<2.0 \times 10^{-13}$
	47.0	<3.2	$<2.1 \times 10^{-13}$
	53.0	<2.6	$<1.7 \times 10^{-13}$
	815.1	<2.1	$<1.4 \times 10^{-13}$
	819.2	<6.2	$<4.0 \times 10^{-13}$
SN 2019xfs	33.4	<4.2	$<2.8 \times 10^{-13}$
	39.1	<3.5	$<2.3 \times 10^{-13}$
	45.9	<6.7	$<4.4 \times 10^{-13}$
	60.8	<6.7	$<4.4 \times 10^{-13}$
	67.3	<3.9	$<2.6 \times 10^{-13}$
	73.2	<3.5	$<2.3 \times 10^{-13}$
	621.8	<3.4	$<2.2 \times 10^{-13}$
SN 2019pud	14.4	<8.8	$<5.6 \times 10^{-13}$
	18.0	<5.9	$<3.7 \times 10^{-13}$
SN 2019uba	9.5	<9.8	$<5.6 \times 10^{-13}$
	13.2	<4.4	$<2.5 \times 10^{-13}$
	15.7	<3.6	$<2.1 \times 10^{-13}$
SN 2019zcr	−13.0	<17.6	$<1.0 \times 10^{-12}$
	−5.5	<6.1	$<3.5 \times 10^{-13}$
	11.0	<8.6	$<5.0 \times 10^{-13}$
	15.6	<9.0	$<5.2 \times 10^{-13}$
	19.4	<5.2	$<3.0 \times 10^{-13}$
	23.0	<6.9	$<4.0 \times 10^{-13}$
	28.6	<9.9	$<5.7 \times 10^{-13}$
	30.4	<19.9	$<1.1 \times 10^{-12}$
	34.4	<32.3	$<1.9 \times 10^{-12}$
	36.9	<20.9	$<1.2 \times 10^{-12}$
	38.7	<13.9	$<8.0 \times 10^{-13}$
	42.9	<12.5	$<7.2 \times 10^{-13}$
	48.1	<24.4	$<1.4 \times 10^{-12}$
SN 2020hgr	−5.3	<6.8	$<4.1 \times 10^{-13}$
	0.9	<9.5	$<5.7 \times 10^{-13}$
	10.7	<18.2	$<1.1 \times 10^{-12}$
	22.9	<34.5	$<2.1 \times 10^{-12}$
	28.0	<7.8	$<4.7 \times 10^{-13}$
	39.2	<5.1	$<3.1 \times 10^{-13}$
SN 2020jhm	24.3	<8.5	$<5.4 \times 10^{-13}$
	28.1	<8.8	$<5.6 \times 10^{-13}$
	37.8	<8.2	$<5.2 \times 10^{-13}$
	480.2	<2.8	$<1.7 \times 10^{-13}$
SN 2020yue	2.7	<6.3	$<3.7 \times 10^{-13}$
	8.5	<8.5	$<5.0 \times 10^{-13}$
	14.2	<13.0	$<7.6 \times 10^{-13}$
	21.7	<6.8	$<4.0 \times 10^{-13}$
	25.6	<6.2	$<3.6 \times 10^{-13}$
	266.5	<4.2	$<2.4 \times 10^{-13}$

APPENDIX C: NOTES ON MOSFIT MAGNETAR MODEL

MOSFIT includes an alternative model for magnetar central engines, labelled `slsn`. This model includes various constraints (for details, see Nicholl et al. 2017) and a modified SED below 3000 Å, emulating the effect of line blanketing common in the UV spectra of SLSNe I (e.g. Yan et al. 2017). In the `magni` model, the SED is simply a blackbody. As established in Section 4.4, neither a simple blackbody nor this modified function with line blanketing can fit four of the six

[17] https://www.swift.ac.uk/user_objects/
[18] https://heasarc.gsfc.nasa.gov/cgi-bin/Tools/w3nh/w3nh.pl
[19] https://heasarc.gsfc.nasa.gov/cgi-bin/Tools/w3nh/w3nh.pl

SEDs in our sample. No major deficit from line blanketing is seen. Therefore we have used the `magni` model in our fits.

For setting a minimum ejecta mass, we conservatively assumed the initial mass of the progenitor was $\gtrsim$14 $M_\odot$; the lowest progenitor mass ascribed to an observed magnetar is, to our knowledge, $\sim$17 $M_\odot$ (Davies et al. 2009). Typically, the initial masses ascribed to millisecond magnetar progenitors are $\gtrsim$30 $M_\odot$ (e.g. Gaensler et al. 2005; Heger, Woosley & Spruit 2005; Olausen & Kaspi 2014). As some hydrogen must be left at the end of the star's life (for SNe II-L, $\sim$1 $M_\odot$ according to Blinnikov & Bartunov 1993), we use the `PARSEC` stellar evolution models[20] (Bressan et al. 2012) to find the final He/CO core mass of an initially 14 $M_\odot$ star assuming Solar metallicity[21]: $\sim$4.5 $M_\odot$. Assuming the entire core mass is still present along with the hydrogen envelope, this results in a final progenitor mass of $\gtrsim$5.5 $M_\odot$. Assuming the maximum mass of the magnetar born in the collapse is $\sim$2.5 $M_\odot$ (Shibata et al. 2019), the minimum ejecta mass was therefore set at 3 $M_\odot$.

[20] http://stev.oapd.inaf.it/cgi-bin/cmd

[21] The core mass increases slightly with lower metallicity; thus assuming Solar metallicity here is the least constraining choice.

This paper has been typeset from a TEX/LATEX file prepared by the author.